UNIVERSITY OF CALIFORNIA
RIVERSIDE

Operation and Intrinsic Error Budget of Two-Qubit Cross-Resonance Gate

A Thesis submitted in partial satisfaction
of the requirements for the degree of

Master of Science

in

Electrical Engineering

by

Vinay Tripathi

March 2019

Thesis Committee:

Professor Alexander Korotkov, Chairperson
Professor Alexander Balandin
Professor Roger Lake

The Thesis of Vinay Tripathi is approved:

Committee Chairperson

University of California, Riverside

Acknowledgments

I am grateful to Sasha, my advisor, without whose help, this work would not have been possible. Sasha has taught me innumerable lessons which have paved the way for my journey to become a physicist. I wish that I could be as patient, energetic, and enthusiastic about research as Sasha. Being his student has been an honor for me, and I hope to continue learning from him in the years to come.

Mostafa was the first person with whom I interacted after joining Sasha's lab. I learned a lot from him about physics, computer programming, and life, in general. No matter what the problem, Mostafa always had a solution for it. I hope that I collaborate with him again in future. I would also like to thank Juan for so many long discussions, I have had with him. Discussing physics with him was nothing less than a treat. His knowledge and dedication towards research was always encouraging and motivating for me.

After joining UCR, I was fortunate enough to be surrounded by many friends. Gauthum, Manjunath, Mayur, Uday, thanks for your friendship, which I am sure would last forever. Riverside would not have been the same place without you all. I would also like to thank my friends in India: Avni, Radhesyam, Vikash, and Vivasha who have always motivated and encouraged me to dream big.

I wouldn't be here without my parents' love and support. I would like to thank them for being there for me whenever I needed and for letting me find my own way. I would also like to thank my brother and sisters who have offered invaluable support and humor over the years.

To my parents for all the support.

ABSTRACT OF THE THESIS

Operation and Intrinsic Error Budget of Two-Qubit Cross-Resonance Gate

by

Vinay Tripathi

Master of Science, Graduate Program in Electrical Engineering
University of California, Riverside, March 2019
Professor Alexander Korotkov, Chairperson

Due to recent developments and accessible fabrication techniques, superconducting qubits have become one of the most popular candidates for realizing a large-scale fault-tolerant quantum computer. Currently, transmon is the most preferred type of superconducting qubits because it is less sensitivity to noise. To perform operations on the qubits, we need quantum gates with high fidelity. One of the high-fidelity two-qubit entangling gates used for superconducting qubits is the Cross-Resonance (CR) gate. In CR gate, two frequency-detuned qubits have a weak coupling and one of them (called control qubit) is driven by a microwave at the frequency of the other qubit (called target). This induces Rabi oscillations of the target qubit, whose frequency depends on the state ($|0\rangle$ and $|1\rangle$) of the control qubit. This entangles the two qubits, thus providing a natural way to realize CNOT gate. In this thesis, we study analytically, semi-analytically and numerically the operation of the Cross-Resonance gate for superconducting qubits to implement the CNOT operation. We also study various intrinsic errors associated with the CR gate.

Chapter 1 of this thesis gives an introduction. In Chapter 2, we discuss the Hamiltonian of the CR gate. In Chapter 3, we first consider the ideal operation of the CR gate, then derive the next-order analytics, and then develop a semi-analytical approach. Chapter 4 gives a description of our numerical model. Numerical results for the CNOT-equivalent gate duration and compensating single-qubit rotations are discussed in Chapter 5. In Chapter 6, we analyze the error budget for the CNOT-gate intrinsic infidelity. In Chapter 7, we discuss the dependence of infidelity and CNOT duration on various parameters including detuning between control and target qubits, drive frequency, coupling between control and target qubit, smoothness of the pulse ramps, and microwave crosstalk. Chapter 8 presents conclusions.

Contents

List of Figures

Chapter 1

Introduction

Richard Feynman came up with an idea of quantum computer, which would use quantum mechanical effects to simulate quantum systems [1], which otherwise could not be simulated even on the most advanced classical computers. This idea was followed up with a series of developments one after the other which inspired and motivated the field of quantum information and computation. Bennet and Brassard with their seminal paper in 1984 introduced the field of quantum cryptography [2]. Deutsch came up with the idea of universal quantum computer [3]. For sometime, this field remained mostly of theoretical interests but with Shor's algorithm for prime factorization on a quantum computer [4, 5], quantum computing reached a wider audience. Another important quantum algorithm was designed by Grover for database search [6]. Shor, Calderbank and Steane proposed the first quantum error correction [7–9] codes which are essential for scalable fault-tolerant quantum computers. Kitaev came up with an idea of topological quantum computing using anyons [10]. Apart from the gate-based models for quantum computing, adiabatic quantum computation has also become popular lately [11, 12].

DiVincenzo gave a set of rules, which any quantum computing implementation must satisfy, popularly known as DiVincenzo criteria [13]. This set of rules put stringent requirements on the type of qubits (quantum bits) which can be used to realize a quantum computer. These requirements include scalability, ease of measurement, ability to initialize the qubits, long coherence time and ability to carry out universal set of gates. Superconducting qubits are among the most popular candidates for the physical implementation of qubits, which not just fulfill all the above requirements but also are relatively easy to build because of the already available semiconductors fabrication techniques.

1.1 Superconducting qubits

A superconducting qubit is essentially an artificial atom having a number of energy levels, which are spaced nonequidistantly. This anharmonicity is introduced by non-linear Josephson junctions [14]. The non-linearity is needed to differentiate between different levels, so that bottom two levels can be used as a qubit. Usually, superconducting qubits are classified into three types, which are charge qubits [15], flux qubits [16, 17], and phase qubits [18, 19]. Each of these types have different advantages over one another. Currently, the most preferred superconducting qubit for gate-based quantum computing is a particular modification of charge qubit, which is less sensitive to charge noise. This is popularly known as the transmon qubit [33], which consists of a Josephson junction shunted with a relatively large capacitor (Fig. 1.1). Transmon is designed in such a way that Josephson energy is much larger than the capacitive energy (roughly 10^2 times).

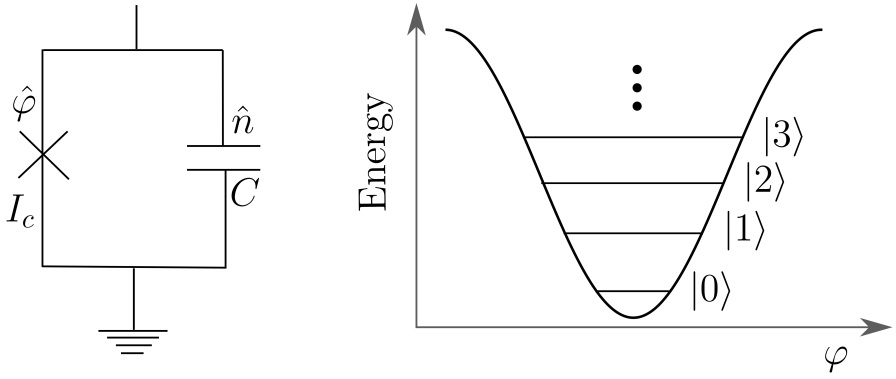

Figure 1.1: Left: Schematic of transmon qubit, consisting of a Josephson junction in parallel with a capacitor. I_c is the Josephson junction critical current, φ is the superconducting phase across the junction, n is the number of Cooper pairs transferred across junction, and C is the capacitance of the capacitor. Right: Cosine potential of transmon with different energy levels. Here, $|0\rangle$ and $1\rangle$ form the qubit.

The Hamiltonian of a transmon qubit is

$$H = -E_J \cos\hat{\varphi} + 4E_{\mathrm{C}}(\hat{n} - n_g)^2, \tag{1.1}$$

where $E_J = I_c\Phi_0/2\pi$ is the Josephson energy, $E_C = e^2/2C$ is the charging energy, I_c is the critical current, $\Phi_0 = h/2e$ is the magnetic flux quantum, $\hat{\varphi}$ is the quantum operator for superconducting phase across Josephson junctions, and $\hat{n}$ is the canonically conjugate operator corresponding to number of Cooper pairs passing through the Josephson junction, where $[\hat{\varphi}, \hat{n}] = i$. Here, n_g is the dimensionless offset charge. The cosine potential in (1.1) causes a small anharmonicity which makes it possible to use transmon as a qubit. There are approximately 9 levels in the potential well of the transmons, where the two lowest levels $|0\rangle$ and $|1\rangle$ form a qubit though all the other higher levels exist and take part in the overall unitary operations. Lower levels of the transmons are almost insensitive to charge noise and therefore a very small decoherence due to background charge fluctuation is observed, thus making transmon a very good qubit.

1.2 Quantum gates

Besides sufficiently good coherence of the qubits, quantum computing applications need high-fidelity gates forming a universal set [36]. Arbitrary one-qubit gates together with any two-qubit entangling gate (like CNOT) can form a universal set of gates. Mathematically, quantum gates are represented by unitary matrices. Any quantum gate acting on n-qubit system is represented by $2^n \times 2^n$ unitary matrix. Some of the notable one-qubit gates are Hadamard (H) gate, X (Pauli σ_x) gate, Y gate, Z gate, etc. Two-qubit entangling gates include Controlled-Z (CZ), CNOT, iSWAP, etc. Single-qubit gates like X and Y gates can be performed by driving the qubits with a microwave pulse. By properly adjusting amplitude, duration, and phase of these pulses, rotations around any arbitrary axis in the x-y plane can be performed. Single-qubit gates with fidelities as high as 99.9% and even more are being implemented routinely [20–22]. Two-qubit gates can be applied to tranmsons using microwave pulses and/or fast dc flux pulses. While single-qubit gates are already considered to be simple and accurate, current fidelity of two-qubit gates also exceeds 99% [26, 37, 38].

1.3 Cross-Resonance gate

One of the high-fidelity two-qubit gates used for superconducting qubits is the Cross-Resonance (CR) gate [39, 40]. In this gate, two frequency-detuned qubits have a fixed coupling (usually via a resonator) and one of them (called control qubit) is driven by a microwave with frequency of the other one (target qubit). This induces Rabi oscillations of the target qubit, whose frequency depends on the state ($|0\rangle$ or $|1\rangle$) of the control qubit, thus

entangling the two qubits and providing a natural way to realize CNOT operation. Since this gate uses only the microwave control, it permits to use the single-junction transmons, thus providing a long coherence time. However, the drawback is a relatively long gate duration compared with the gates based on tune-detune operation [37].

The idea of the CR gate was proposed in 2006 in Ref. [41] and then experimentally implemented for flux qubits in 2010 in Ref. [42] under the name of Selective Darkening (the difference compared with a simple CR gate is an additional active cancellation pulse applied to the target qubit). The CR terminology was introduced in 2010 in the theoretical paper [39] and the first experiment under this name was realized for phase qubits in 2011 in Ref. [40] with fidelity of 81%. In 2012 the CR gate was applied to transmons [43], with resulting fidelity of 95%. Since that time the CR gate was used in numerous experiments by several groups (e.g.,[24,38,44–48]), with gradual increase of maximum fidelity. An important improvement of the CR operation was achieved by using the echo sequence [44, 46], which not only increases fidelity, but also permits to avoid compensating one-qubit rotations in implementation of the CNOT gate. The CR gate with duration of 160 ns and fidelity of 99.1% reported in Ref. [38] was achieved by using both the echo sequence and active cancellation pulses applied to the target qubit. In spite of an extensive experimental use of the CR gate, its theoretical analysis has been rather limited. Besides the initial papers [39,41] outlying the main idea, the CR gate was analyzed in Ref. [49] with an account of the next level, briefly mentioned in Ref. [50], and analyzed in detail in recent paper [51]. There were also numerical studies [52,53] and related papers [54,55].

In this thesis, we analyze operation of the basic CR gate for transmons (using simple pulse shapes without echo sequences) at three levels of accuracy: analytical, semi-analytical, and numerical. This thesis is organized as follows. In Chapter 2, we discuss the system and its Hamiltonian. In Chapter 3, we first consider the ideal operation of the CR gate, then derive the next-order analytics, and then develop the semi-analytical approach. The numerical method is discussed in Chapter 4. Numerical results for the CNOT-equivalent gate duration and compensating single-qubit rotations are discussed in Chapter 5. Then in Chapter 6, we analyze the error budget for the CNOT-gate intrinsic infidelity. In Chapter 7, we discuss dependence of CNOT duration and infidelity on parameters. Finally, we conclude in Chapter 8.

Chapter 2

System and Hamiltonian

In the CR gate, the control and target qubits (with frequencies ω_c and ω_t, respectively) are usually detuned by 50–300 MHz and are permanently coupled via a resonator. However, for simplicity in this thesis we will consider a direct qubit-qubit coupling g (Fig. 2.1) since the usual analysis of the CR gate [50, 51] also reduces the coupling via a resonator to an effective direct coupling. For the CR operation, the control qubit is rf-driven at the frequency of the target qubit, $\omega_d \approx \omega_t$. This produces an effective drive (x-rotation) of the target qubit, with the strength depending on the state of the control qubit. Such a process can be naturally used to realize the CNOT gate by calibrating the target-qubit rotation angle difference (between rotations for the control-qubit states $|0\rangle$ and $|1\rangle$) to be equal to π and somehow compensating the target-qubit rotation for the control-qubit state $|0\rangle$. This compensation can be done, for example, by using the echo sequence [38, 44, 46] or active cancellation [38, 42]; however, in this thesis we will assume that the compensation is done afterwards [39, 40] by applying single-qubit rotations. We intentionally consider the

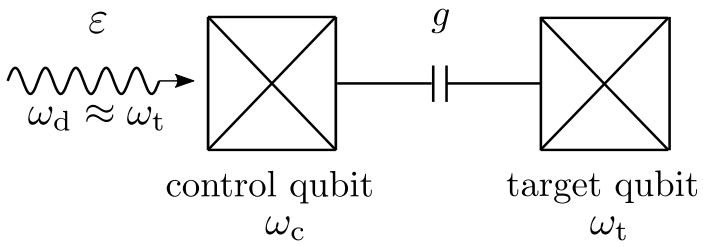

Figure 2.1: Schematic of the CR gate: detuned control and target qubits (transmons with frequencies ω_c and ω_t) have coupling g, and the control qubit is microwave-driven at the frequency of the target qubit, $\omega_\mathrm{d} \approx \omega_\mathrm{t}$. The microwave drive amplitude is ε.

simplest case in order to focus on developing a good understanding of the basic operation of the CR gate.

2.1 Classical understanding

The operating principle of the CR gate can be understood classically, by replacing qubits with classical oscillators (Fig. 2.2). Since the drive is off-resonance with the control-oscillator ($\omega_\mathrm{d} \not\approx \omega_\mathrm{c}$), it will produce very small forced oscillations at the drive frequency ω_d. However, since the target-oscillator is on-resonance with this frequency ($\omega_\mathrm{d} \approx \omega_\mathrm{t}$), it will still get excited via the coupling g with the control-oscillator. Note that if the control-oscillator is linear, then its own state (its oscillation with frequency ω_c) does not matter because of linearity. However, if the control-oscillator is nonlinear, then its effective frequency depends on its own state (i.e., amplitude of ω_c-oscillations); therefore, the amplitude of the small forced oscillations of the control-oscillator and consequently the excitation rate of the target-oscillator will depend on the control-oscillator state. This simple classical picture explains the basic physical mechanism of the CR gate operation for transmons, which are slightly nonlinear oscillators. It also explains why the CR gate speed depends on nonlinearity of

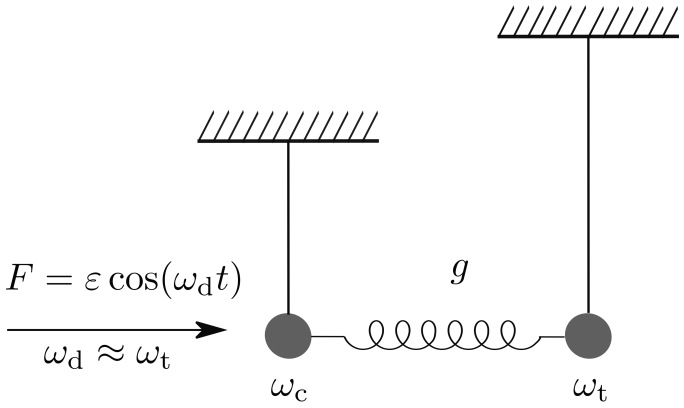

Figure 2.2: Classical CR gate counterpart: two coupled nonlinear oscillators, with the one oscillator driven by a periodic force F on resonance with the other oscillator.

the control qubit and practically does not depend on the target-qubit nonlinearity.

2.2 Hamiltonian

For quantum analysis of the CR gate (Fig. 2.1), let us start with the rotating-frame Hamiltonian (the rotating frame is based on the drive frequency $\omega_{\rm d}$)

$$H = H_{\rm qb} + H_g + H_\varepsilon, \tag{2.1}$$

where $H_{\rm qb}$ describes two uncoupled transmon qubits, H_g describes their coupling, and H_ε describes the microwave drive on the control qubit.

The uncoupled-qubit part can be written as

$$H_{\rm qb} = \sum\nolimits_{n,m} (E_n^{\rm (c)} + E_m^{\rm (t)})\, |n,m\rangle\langle n,m|, \tag{2.2}$$

$$E_n^{\rm (c)} = E_n^{\rm (c,\,lf)} - n\omega_{\rm d}, \;\; E_m^{\rm (t)} = E_m^{\rm (t,\,lf)} - m\omega_{\rm d}, \tag{2.3}$$

where in the notation $|n,m\rangle$ the control-qubit state is at the left ($n = 0, 1, 2, ...$) and the target-qubit state is at the right ($m = 0, 1, 2, ...$), the control-qubit energies $E_n^{\rm (c)}$ in the

rotating frame are related to the laboratory-frame energies $E_n^{(\mathrm{c},\,\mathrm{lf})}$ via the drive frequency ω_d, and there is a similar relation for the target-qubit energies $E_m^{(\mathrm{t})}$. We set $E_0^{(\mathrm{c})} = E_0^{(\mathrm{t})} = 0$. For the energies $E_n^{(\mathrm{c})}$ and $E_m^{(\mathrm{t})}$, in this thesis we will use the Duffing (Kerr) oscillator approximation,

$$E_n^{(\mathrm{c})} = n(\Delta + \delta) - \frac{n(n-1)}{2}\,\eta_\mathrm{c}, \tag{2.4}$$

$$E_m^{(\mathrm{t})} = m\delta - \frac{m(m-1)}{2}\,\eta_\mathrm{t}, \tag{2.5}$$

$$\Delta \equiv \omega_\mathrm{c} - \omega_\mathrm{t}, \;\; \delta \equiv \omega_\mathrm{t} - \omega_\mathrm{d} \approx 0, \tag{2.6}$$

where Δ is the detuning between the qubits, while η_c and η_t are anharmonicities of the control and target qubits, respectively (for transmons $\eta_\mathrm{c} > 0$ and $\eta_\mathrm{t} > 0$). A small mismatch δ between the drive frequency ω_d and the *bare* frequency ω_t of the target qubit can be used, e.g., to make the drive exactly resonant with the hybridized target qubit for the control-qubit states $|0\rangle$ or $|1\rangle$ (or in between). Note that $\Delta + \delta = \omega_\mathrm{c} - \omega_\mathrm{d}$. Instead of the approximation (2.4)–(2.6), it is possible to use numerical results for the transmon energies or at least the improved approximation [57, 58]. However, we prefer the simple approximation for easier comparison with previous theoretical analyses of the CR gate.

The qubit-qubit coupling Hamiltonian H_g in general couples all pairs of the bare states $|n, m\rangle$ and $|n', m'\rangle$. However, in this thesis we use the simplest (traditional) approximation for transmons by keeping only the RWA terms and using the matrix elements for linear oscillators,

$$H_g = \sum\nolimits_{n,m} g\,\sqrt{nm}\,|n, m-1\rangle\langle n-1, m| + \mathrm{h.c.}, \tag{2.7}$$

additionally assuming (without loss of generality) that the coupling constant g is real. Similarly, we use the linear-oscillator matrix elements for the drive Hamiltonian (in the

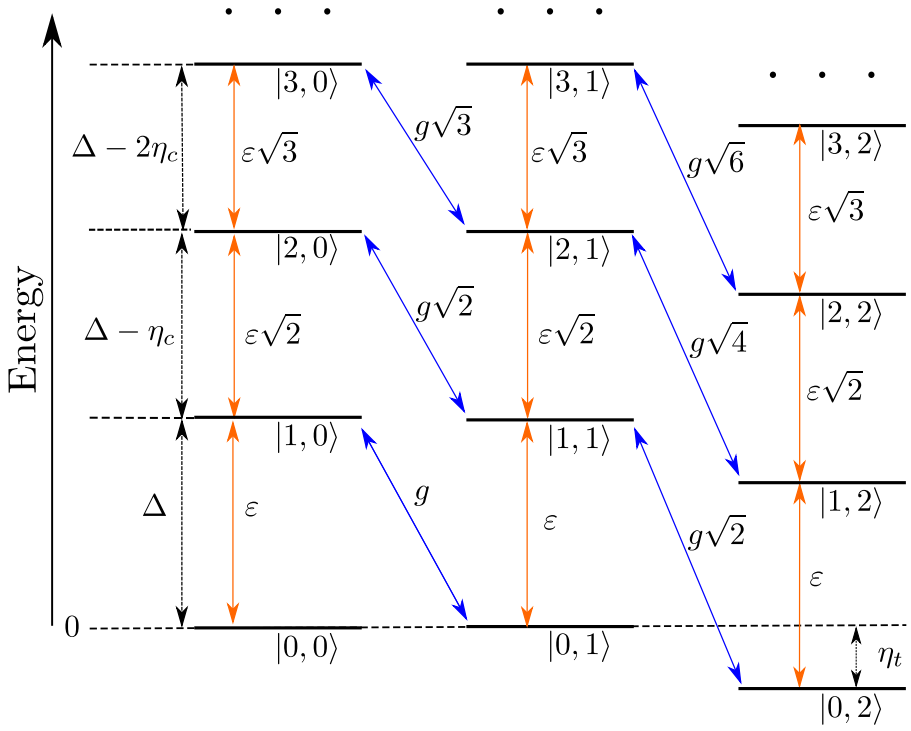

Figure 2.3: Diagram of bare energy levels for the CR gate: each vertical ladder is for the control-qubit states, with a fixed state of the target qubit. Tilted blue lines illustrate coupling between the bare levels due to the qubit-qubit coupling H_g, orange lines are due to the drive Hamiltonian H_ε. On this diagram we assumed $\delta = 0$ (a non-zero δ would produce an energy shift between the ladders; also, in this case Δ should be replaced with $\Delta + \delta$). Control-qubit states above $|3\rangle$ and target-qubit states above $|2\rangle$ are not shown.

rotating frame),

$$H_\varepsilon = \sum\nolimits_n \varepsilon(t)\,\sqrt{n}\,|n,m\rangle\langle n-1,m| + \text{h.c.}, \tag{2.8}$$

where the complex amplitude ε of the drive depends on time, so that $\varepsilon(t)$ is the pulse shape of the CR gate, with $\varepsilon(t) = 0$ before and after the gate. Instead of Hamiltonians (2.7) and (2.8), it is possible to use improved perturbative Hamiltonians [57, 58] or numerical matrix elements for transmons, but in this thesis we will use the simple traditional approximation. Here we do not consider the microwave crosstalk [38, 40, 43, 51]; however, it will be added in Chapter 7.

It is convenient to draw a diagram (Fig. 2.3) of bare levels $|n,m\rangle$, in which the left ladder of levels corresponds to the target-qubit state $|0\rangle$ ($m = 0$), the next ladder corresponds to the target-qubit state $|1\rangle$, then $|2\rangle$, and so on. Note that for $\delta = 0$, the left two ladders are at exactly equal energies. In Fig. 2.3 the coupling H_g is represented by slanted blue arrows and the drive H_ε corresponds to vertical orange arrows. For clarity, in Fig. 2.3 we show the case $\Delta > 2\eta_\mathrm{c}$, while in experiments usually $0 < \Delta < \eta_\mathrm{c}$. In such a case, all ladders turn down after the states $|1,m\rangle$ and the diagram becomes visually complicated, so for gaining intuition it is easier to use the case of Fig. 2.3.

Besides the bare states $|n,m\rangle$, we will also use the eigenstates of the Hamiltonian $H_\mathrm{qb} + H_g$ (without the drive), which we denote with the overline: $\overline{|n,m\rangle}$. The coupling H_g affects the qubit frequencies, so instead of the bare frequency ω_t of the target qubit, we have two eigenfrequencies: $\omega_\mathrm{t}^{\mathrm{c}0}$ and $\omega_\mathrm{t}^{\mathrm{c}1}$, depending on the control-qubit state ($|0\rangle$ and $|1\rangle$, respectively). They can be calculated as

$$\omega_\mathrm{t}^{\mathrm{c}0} = E^{(\mathrm{lf})}_{\overline{|0,1\rangle}} - E^{(\mathrm{lf})}_{\overline{|0,0\rangle}}, \quad \omega_\mathrm{t}^{\mathrm{c}1} = E^{(\mathrm{lf})}_{\overline{|1,1\rangle}} - E^{(\mathrm{lf})}_{\overline{|1,0\rangle}}, \tag{2.9}$$

where $E^{(\mathrm{lf})}_{\overline{|n,m\rangle}}$ is the laboratory-frame eigenenergy of the state $\overline{|n,m\rangle}$. We will call "zz-coupling" the difference between these frequencies,

$$\omega_{zz} \equiv \omega_\mathrm{t}^{\mathrm{c}1} - \omega_\mathrm{t}^{\mathrm{c}0} = E_{\overline{|11\rangle}} + E_{\overline{|00\rangle}} - E_{\overline{|01\rangle}} - E_{\overline{|10\rangle}}, \tag{2.10}$$

where this combination of eigenenergies is the same in the laboratory and rotating frames. The zz-coupling is mainly due to repulsion of the energy level $|11\rangle$ from the levels $|02\rangle$ and $|20\rangle$, which gives the approximate value

$$\omega_{zz} \approx \frac{2g^2}{\Delta + \eta_\mathrm{t}} - \frac{2g^2}{\Delta - \eta_\mathrm{c}}. \tag{2.11}$$

From Eq. (2.10) we see that the zz-coupling can be also defined as $\omega_{zz} = \omega_{\mathrm{c}}^{\mathrm{t}1} - \omega_{\mathrm{c}}^{\mathrm{t}0}$, where $\omega_{\mathrm{c}}^{\mathrm{t}0}$ and $\omega_{\mathrm{c}}^{\mathrm{t}1}$ are the eigenfrequencies of the control qubit for the target-qubit states $|0\rangle$ and $|1\rangle$, respectively. Nonzero ω_{zz} will be important for numerical results; however, it will be neglected for analytical and semi-analytical results in the next chapter; in particular, we will not distinguish between $\omega_{\mathrm{t}}^{\mathrm{c}0}$, $\omega_{\mathrm{t}}^{\mathrm{c}1}$, and ω_{t}.

Chapter 3

Basic analytical and semi-analytical analysis

3.1 Ideal CR gate operation

There is no drive, $\varepsilon = 0$, before and after the CR gate operation. Therefore, the initial and final two-qubit states should be considered in the eigenbasis $\overline{|n,m\rangle}$ of the Hamiltonian $H_{\rm qb} + H_g$. The drive Hamiltonian H_ε couples these eigenstates, providing an evolution used in the CR gate.

As follows from Fig. 2.3, in the rotating frame based on the drive frequency $\omega_{\rm d}$, there is a near-resonance condition between states $|n,0\rangle$ and $|n,1\rangle$, which leads to a near-resonance between eigenstates $\overline{|n,0\rangle}$ and $\overline{|n,1\rangle}$, while other pairs of states are off resonance. Therefore, as long as perturbation produced by H_ε is small enough, it effectively couples only states $\overline{|n,0\rangle}$ and $\overline{|n,1\rangle}$, and for the ideal effective Hamiltonian $H_{\rm CR}^{\rm ideal}$ of the CR gate we can write

$$H_{\rm CR}^{\rm ideal} - (H_{\rm qb} + H_g) = \big(\tilde{\varepsilon}_0 \overline{|0,1\rangle}\ \overline{\langle 0,0|} + \tilde{\varepsilon}_1 \overline{|1,1\rangle}\ \overline{\langle 1,0|}$$

$$+\tilde{\varepsilon}_2 \overline{|2,1\rangle}\ \overline{\langle 2,0|} + ...\big) + \text{h.c.}, \tag{3.1}$$

where $\tilde{\varepsilon}_0$ is the amplitude of the *effective drive on the target qubit* when the control qubit is $|0\rangle$, $\tilde{\varepsilon}_1$ is the effective drive amplitude for the control-qubit state $|1\rangle$, etc. (for small g there is almost no difference between the drive in the bare basis or eigenbasis). The effective drive amplitudes $\tilde{\varepsilon}_n$ depend on the actual drive amplitude ε (in the perturbative case being proportional to ε).

Note that if we are interested only in the states $|0\rangle$ and $|1\rangle$ of the control qubit, then in the widely used terminology [40, 43, 47, 51] the effective Hamiltonian (3.1) can be written as

$$\frac{\tilde{\varepsilon}_0 - \tilde{\varepsilon}_1}{2}\, Z_{\rm c} X_{\rm t} + \frac{\tilde{\varepsilon}_0 + \tilde{\varepsilon}_1}{2}\, I_{\rm c} X_{\rm t},$$

where the Pauli operators $Z_{\rm c}$ and $I_{\rm c}$ act on the control qubit and the operator $X_{\rm t}$ acts on the target qubit (here we assume real $\tilde{\varepsilon}_0$ and $\tilde{\varepsilon}_1$; otherwise we also need $Y_{\rm t}$). The CNOT gate can be realized with this effective interaction by applying the drive pulse with duration $\tau_{\rm p}$, satisfying the condition

$$\int_0^{\tau_{\rm p}} [2\tilde{\varepsilon}_0(t) - 2\tilde{\varepsilon}_1(t)]\, dt = \pi, \tag{3.2}$$

complemented with two one-qubit rotations. The additional x-rotation of the target qubit over the angle $-\int_0^{\tau_{\rm p}} 2\tilde{\varepsilon}_0(t)\, dt$ compensates the target-qubit rotation for the control-qubit state $|0\rangle$, also providing x-rotation over angle π for the control-qubit state $|1\rangle$. Besides the x-rotation of the target qubit, the control qubit should be z-rotated over the angle $\pi/2$

(relative to the rotating frame of the control qubit). This is needed because the x-rotation of the target qubit over angle π produces the operation $-iX$ instead of the desired (for CNOT) operation X, thus requiring additional phase factor i for the control-qubit state $|1\rangle$ (the same factor exists in a one-qubit X gate, but it is not important since it is an overall phase, in contrast to the phase difference in a controlled two-qubit operation). Note that the factors of 2 in Eq. (3.2) are needed because the Rabi frequency is twice bigger than the drive matrix element in the Hamiltonian.

The effective drive amplitudes $\tilde{\varepsilon}_n$ in Eq. (3.1) can be easily found (in the ideal lowest-order case) by comparing Eqs. (2.1) and (3.1), which gives

$$\tilde{\varepsilon}_n = \overline{\langle n,1|} H_\varepsilon \overline{|n,0\rangle}. \tag{3.3}$$

To calculate $\tilde{\varepsilon}_n$ in the lowest order, let us assume $\delta = 0$, i.e., the drive resonant with the bare target qubit (the difference between bare and eigenfrequencies is not important for these approximate calculations). Then using $\overline{|0,0\rangle} = |0,0\rangle$ (see Fig. 2.3) and the first-order approximation $\overline{|0,1\rangle} = |0,1\rangle - (g/\Delta)\,|1,0\rangle$ (normalization correction is of the second order), we find the linear approximation

$$\tilde{\varepsilon}_0 = -\frac{g}{\Delta}\,\varepsilon. \tag{3.4}$$

Similarly, using the first-order approximations $\overline{|1,0\rangle} = |1,0\rangle + (g/\Delta)\,|0,1\rangle$ and $\overline{|1,1\rangle} = |1,1\rangle - [\sqrt{2}\,g/(\Delta-\eta_\mathrm{c})]\,|2,0\rangle + [\sqrt{3}\,g/(\Delta+\eta_\mathrm{t})]\,|0,2\rangle$ (see Fig. 2.3), we obtain approximation

$$\tilde{\varepsilon}_1 = \frac{g}{\Delta}\,\varepsilon - \frac{\sqrt{2}\,g}{\Delta-\eta_\mathrm{c}}\,\sqrt{2}\,\varepsilon = -\frac{g}{\Delta}\,\frac{\Delta+\eta_\mathrm{c}}{\Delta-\eta_\mathrm{c}}\,\varepsilon. \tag{3.5}$$

Also similarly, using approximations $\overline{|2,0\rangle} = |2,0\rangle + [\sqrt{2}\,g/(\Delta-\eta_{\rm c})]\,|1,1\rangle$ and $\overline{|2,1\rangle} = |2,1\rangle - [\sqrt{3}\,g/(\Delta-2\eta_{\rm c})]\,|3,0\rangle + [2g/(\Delta-\eta_{\rm c}+\eta_{\rm t})]\,|1,2\rangle$, we find

$$\begin{aligned}\tilde{\varepsilon}_2 &= \frac{\sqrt{2}\,g}{\Delta-\eta_{\rm c}}\,\sqrt{2}\,\varepsilon - \frac{\sqrt{3}\,g}{\Delta-2\eta_{\rm c}}\,\sqrt{3}\,\varepsilon \\ &= -\frac{g(\Delta+\eta_{\rm c})}{(\Delta-\eta_{\rm c})(\Delta-2\eta_{\rm c})}\,\varepsilon,\end{aligned} \tag{3.6}$$

and for an arbitrary control-qubit state $|n\rangle$, within the model (2.1)–(2.8) we obtain

$$\begin{aligned}\tilde{\varepsilon}_n &= \frac{ng\varepsilon}{\Delta-(n-1)\eta_{\rm c}} - \frac{(n+1)g\varepsilon}{\Delta-n\eta_{\rm c}} \\ &= -\frac{g(\Delta+\eta_{\rm c})}{[\Delta-(n-1)\eta_{\rm c}](\Delta-n\eta_{\rm c})}\,\varepsilon.\end{aligned} \tag{3.7}$$

Since the target-qubit rotation for the control-qubit state $|0\rangle$ is usually compensated, most important are the differences of effective drive amplitudes from $\tilde{\varepsilon}_0$, e.g.,

$$\tilde{\varepsilon}_1 - \tilde{\varepsilon}_0 = \frac{2g\eta_{\rm c}}{\Delta(\eta_{\rm c}-\Delta)}\,\varepsilon, \tag{3.8}$$

$$\tilde{\varepsilon}_2 - \tilde{\varepsilon}_0 = \frac{2g\eta_{\rm c}(\eta_{\rm c}-2\Delta)}{\Delta(\eta_{\rm c}-\Delta)(2\eta_{\rm c}-\Delta)}\,\varepsilon. \tag{3.9}$$

Note that these formulas depend on anharmonicity $\eta_{\rm c}$ of the control qubit but do not depend on the target-qubit anharmonicity $\eta_{\rm t}$. Also, for $\eta_{\rm c} = 0$ we have $\tilde{\varepsilon}_n = \tilde{\varepsilon}_0 = -(g/\Delta)\varepsilon$. These properties are in agreement with the classical description of the CR gate operation discussed above.

Language of virtual-state transitions

Instead of using Eq. (3.3), we can find the effective drive amplitudes $\tilde{\varepsilon}_n$ (still in the first order) using the ideology of transitions via a virtual state. As seen in Fig. 2.3, it is possible to go from the state $|0,0\rangle$ to the resonant state $|0,1\rangle$ in two jumps:

$|0,0\rangle \to |1,0\rangle \to |0,1\rangle$, which have transition amplitudes (matrix elements) ε and g, with the intermediate state separated by the energy difference Δ. Therefore, the amplitude of this transition (effective coupling between states $|0,0\rangle$ and $|0,1\rangle$) is

$$\tilde{\varepsilon}_0 = \varepsilon \, \frac{-1}{\Delta} \, g, \tag{3.10}$$

which coincides with Eq. (3.4).

For the transition between states $|1,0\rangle$ and $|1,1\rangle$, there are two two-jump paths: via the state $|2,0\rangle$ (which is higher in energy by $\Delta - \eta_c$) and via $|0,1\rangle$ (which is lower in energy by Δ). Adding these two amplitudes, we obtain

$$\tilde{\varepsilon}_1 = \sqrt{2}\,\varepsilon \, \frac{-1}{\Delta - \eta_c} \, \sqrt{2}\, g + g \, \frac{-1}{-\Delta} \, \varepsilon, \tag{3.11}$$

which coincides with Eq. (3.5).

Similarly, adding the amplitudes for the paths $|n,0\rangle \to |n+1,0\rangle \to |n,1\rangle$ and $|n,0\rangle \to |n-1,1\rangle \to |n,1\rangle$, we obtain

$$\tilde{\varepsilon}_n = -\frac{\sqrt{n+1}\,\varepsilon \, \sqrt{n+1}\, g}{\Delta - n\eta_c} + \frac{\sqrt{n}\, g \, \sqrt{n}\, \varepsilon}{\Delta - (n-1)\eta_c}, \tag{3.12}$$

which coincides with Eq. (3.7).

3.2 Next-order analytics

Numerical results for the effective drive amplitudes $\tilde{\varepsilon}_n$ (discussed later) show that $\tilde{\varepsilon}_n$ is proportional to the actual drive amplitude ε [as expected from Eq. (3.7)] only in some range of ε values. A minor deviation from the linearity at very small ε (discussed later) is due to dependence of the target-qubit frequency on the control-qubit state – see Eq. (2.10).

The deviation from linearity at large ε is much more important for practice since it makes impossible to shorten the CNOT gate duration beyond some value by simply increasing the drive amplitude.

In order to understand the reason for the deviation from linearity at large ε, in this chapter we develop the next-order analytics for $\tilde{\varepsilon}_0$ and $\tilde{\varepsilon}_1$, which gives corrections compared with Eqs. (3.4) and (3.5). Note that a similar next-order analytics has been developed in Ref. [51]; however, a different result was obtained (our numerical calculations confirm our result).

The simple analytics (3.4)–(3.7) has been obtained from Eq. (3.3), which treats the drive Hamiltonian H_ε as a small perturbation. However, for a large drive amplitude ε, the eigenbasis of $H_{\rm qb}+H_g$ is no longer the appropriate eigenbasis; instead, $H_{\rm qb}+H_\varepsilon$ is the main Hamiltonian, while H_g is the perturbation. Note that in the linear approximation the same $\tilde{\varepsilon}_n$ as in Eq. (3.3) can be obtained by exchanging the roles of H_g and H_ε, i.e., by using

$$\tilde{\varepsilon}_n = \overline{{}_\varepsilon\langle n,1)|}H_g\overline{|n,0\rangle_\varepsilon}, \tag{3.13}$$

where $\overline{|n,m\rangle_\varepsilon}$ denotes the eigenstate of $H_{\rm qb}+H_\varepsilon$. This equivalence is clear from the discussed above approach of virtual-state transitions, which treats H_g and H_ε on equal footing.

For a large ε, Eq. (3.13) is more appropriate than Eq. (3.3) to calculate $\tilde{\varepsilon}_n$. Even though the initial and final states should still be treated in the eigenbasis of $H_{\rm qb}+H_g$, during the front and rear ramps of the microwave pulse the appropriate eigenbases essentially transform into each other, leading to Eq. (3.13). While we do not have a rigorous justification of the approximation (3.13) (only a general understanding in the spirit of the adiabatic theorem), numerical results confirm its good accuracy.

Since for the eigenstates $\overline{|n,m\rangle_\varepsilon}$ used in Eq. (3.13) the ladders in Fig. 2.3 are uncoupled, we can write

$$\overline{|n,0\rangle_\varepsilon} = \overline{|n\rangle_\varepsilon}\,|0\rangle_\mathrm{t}, \quad \overline{|n,1\rangle_\varepsilon} = \overline{|n\rangle_\varepsilon}\,|1\rangle_\mathrm{t}, \tag{3.14}$$

where $\overline{|n\rangle_\varepsilon}$ are the control-qubit eigenstates, which account for the drive. They satisfy the Schrödinger equation

$$H^{(\mathrm{c})}_{\mathrm{qb}+\varepsilon}\,\overline{|n\rangle_\varepsilon} = E_{\overline{|n\rangle_\varepsilon}}\,\overline{|n\rangle_\varepsilon} \tag{3.15}$$

with the Hamiltonian for only the control qubit,

$$H^{(\mathrm{c})}_{\mathrm{qb}+\varepsilon} = \sum_n E^{(\mathrm{c})}_n |n\rangle\langle n| + \sqrt{n}\,(\varepsilon\,|n\rangle\langle n-1| + \varepsilon^*|n-1\rangle\langle n|). \tag{3.16}$$

Then solving this Schrödinger equation and finding the eigenstates,

$$\overline{|n\rangle_\varepsilon} = \sum\nolimits_k c^{(n)}_k |k\rangle, \tag{3.17}$$

we find the effective drive amplitudes $\tilde{\varepsilon}_n$ from Eq. (3.13) as (see Fig. 2.3)

$$\tilde{\varepsilon}_n = g \sum\nolimits_k \sqrt{k}\, c^{(n)}_k \left(c^{(n)}_{k-1}\right)^*. \tag{3.18}$$

Let us use this approach to find $\tilde{\varepsilon}_0$ up to the order ε^3 [instead of ε^1 in the linear approximation (3.4)], treating H_ε as a perturbation of H_qb. The eigenstate $\overline{|0\rangle_\varepsilon}$ of the control qubit can be written as

$$\overline{|0\rangle_\varepsilon} = \frac{|0\rangle + \alpha\,|1\rangle + \beta\,|2\rangle + \gamma\,|3\rangle + \ldots}{\mathcal{N}}, \tag{3.19}$$

where $\mathcal{N}$ is a normalization. Substituting this form into the Schrödinger equation (3.15)

and equating the coefficients for the basis states $|0\rangle$, $|1\rangle$, and $|2\rangle$, we obtain

$$\varepsilon\alpha = E, \tag{3.20}$$

$$E_1\alpha + \sqrt{2}\,\varepsilon\,\beta + \varepsilon = E\,\alpha, \tag{3.21}$$

$$E_2\beta + \sqrt{2}\,\varepsilon\,\alpha + \sqrt{3}\,\varepsilon\,\gamma = E\,\beta, \tag{3.22}$$

where for brevity $E = E_{\overline{|0\rangle_\varepsilon}}$, $E_n = E_n^{(c)}$, we used $E_0 = 0$ [as in Eq. (2.4)] and also assumed that ε is real.

In the lowest order, assuming small ε (therefore $\gamma \ll \beta \ll \alpha$ and $E \approx 0$) we crudely find

$$\alpha \approx \frac{-\varepsilon}{E_1}, \quad \beta \approx \frac{-\sqrt{2}\,\varepsilon\,\alpha}{E_2} \approx \frac{\sqrt{2}\,\varepsilon^2}{E_1 E_2}, \quad E \approx \frac{-\varepsilon^2}{E_1}. \tag{3.23}$$

Using these values for β and E in Eq. (3.21), we obtain a better approximation (up to ε^3) for α:

$$\alpha \approx -\frac{\varepsilon(1 + 2\varepsilon^2/E_1E_2)}{E_1 + \varepsilon^2/E_1} \approx -\frac{\varepsilon}{E_1}\left(1 + \frac{2\varepsilon^2}{E_1E_2} - \frac{\varepsilon^2}{E_1^2}\right). \tag{3.24}$$

To find $\tilde{\varepsilon}_0$ with accuracy up to ε^3, we need α with accuracy up to ε^3, β with accuracy up to ε^2 and $\mathcal{N}$ with accuracy up to ε^2, while γ is not needed [see Eq. (3.18)]. Thus, we use Eq. (3.24) for α, Eq. (3.23) for β, and $\mathcal{N} \approx 1 + (\varepsilon/E_1)^2/2$ to obtain

$$\begin{aligned}\overline{|0\rangle_\varepsilon} \approx \left(1 - \frac{\varepsilon^2}{2E_1^2}\right)|0\rangle - \frac{\varepsilon}{E_1}\left(1 + \frac{2\varepsilon^2}{E_1E_2} - \frac{3\varepsilon^2}{2E_1^2}\right)|1\rangle \\ + \frac{\sqrt{2}\,\varepsilon^2}{E_1E_2}\,|2\rangle.\end{aligned} \tag{3.25}$$

The energy of state $\overline{|0\rangle_\varepsilon}$ (not needed for this derivation but needed later) is

$$E_{\overline{|0\rangle_\varepsilon}} = \varepsilon\alpha \approx -\frac{\varepsilon^2}{E_1}\left(1 + \frac{2\varepsilon^2}{E_1E_2} - \frac{\varepsilon^2}{E_1^2}\right). \tag{3.26}$$

Finally, using Eqs. (3.18) and (3.25), we obtain

$$\tilde{\varepsilon}_0 = -g\,\frac{\varepsilon}{E_1}\left(1 - \frac{2\varepsilon^2}{E_1^2} + \frac{4\varepsilon^2}{E_1 E_2}\right) \tag{3.27}$$

with accuracy up to ε^3. Note that $E_1 = E_1^{(\mathrm{c})} = \Delta + \delta$, $E_2 = E_2^{(\mathrm{c})} = 2(\Delta + \delta) - \eta_{\mathrm{c}}$, and we can neglect δ (i.e., use $\delta = 0$). For a complex ε, we need to replace ε^2 in parentheses with $|\varepsilon|^2$.

Calculation of $\tilde{\varepsilon}_1$ up to the order ε^3 is similar and requires finding $\overline{|1\rangle_\varepsilon}$. Note that the calculations are easier if the energies are counted from E_1, since in this case the eigenenergy E in equations similar to Eqs. (3.20)–(3.22) is small. The calculations give

$$\begin{aligned}
\overline{|1\rangle_\varepsilon} \approx{}& \left(1 - \frac{\varepsilon^2}{2E_{01}^2} - \frac{\varepsilon^2}{E_{21}^2}\right)|1\rangle \\
&- \frac{\sqrt{2}\,\varepsilon}{E_{21}}\left(1 + \frac{3\varepsilon^2}{E_{21}E_{31}} - \frac{\varepsilon^2}{E_{01}E_{21}} - \frac{3\varepsilon^2}{E_{21}^2} - \frac{\varepsilon^2}{2E_{01}^2}\right)|2\rangle \\
&- \frac{\varepsilon}{E_{01}}\left(1 - \frac{3\varepsilon^2}{2E_{01}^2} - \frac{2\varepsilon^2}{E_{01}E_{21}} - \frac{\varepsilon^2}{E_{21}^2}\right)|0\rangle + \frac{\sqrt{6}\,\varepsilon^2}{E_{21}E_{31}}|3\rangle,
\end{aligned} \tag{3.28}$$

where $E_{nn'} \equiv E_n - E_{n'} = E_n^{(\mathrm{c})} - E_{n'}^{(\mathrm{c})}$. The corresponding energy is

$$\begin{aligned}
E_{\overline{|1\rangle_\varepsilon}} \approx{}& E_1 - \frac{\varepsilon^2}{E_{01}}\left(1 - \frac{\varepsilon^2}{E_{01}^2} - \frac{2\varepsilon^2}{E_{21}E_{01}}\right) \\
&- \frac{2\varepsilon^2}{E_{21}}\left(1 + \frac{3\varepsilon^2}{E_{21}E_{31}} - \frac{2\varepsilon^2}{E_{21}^2} - \frac{\varepsilon^2}{E_{01}E_{21}}\right).
\end{aligned} \tag{3.29}$$

Using Eqs. (3.18) and (3.28), we obtain

$$\begin{aligned}
\tilde{\varepsilon}_1 = {}& -\frac{2\varepsilon g}{E_{21}}\left(1 + \frac{6\varepsilon^2}{E_{21}E_{31}} + \frac{\varepsilon^2}{E_{10}E_{21}} - \frac{4\varepsilon^2}{E_{21}^2} - \frac{\varepsilon^2}{E_{10}^2}\right) \\
&+ \frac{\varepsilon g}{E_{10}}\left(1 - \frac{2\varepsilon^2}{E_{10}^2} + \frac{2\varepsilon^2}{E_{10}E_{21}} - \frac{2\varepsilon^2}{E_{21}^2}\right)
\end{aligned} \tag{3.30}$$

with accuracy up to ε^3 (note the use of E_{10} instead of E_{01} in the preceding formulas). In

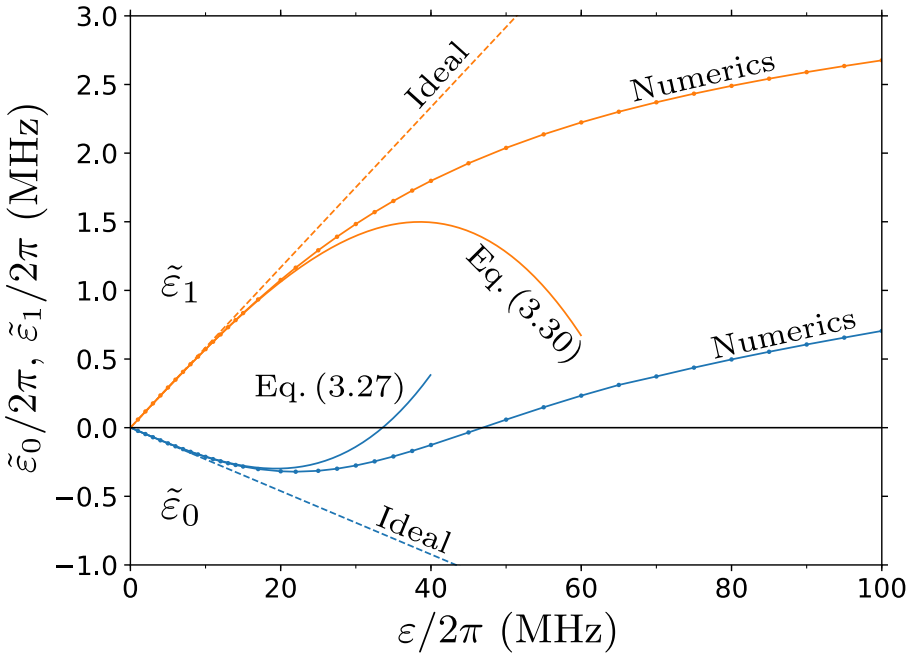

Figure 3.1: The effective drive amplitudes $\tilde{\varepsilon}_0$ (blue lines) and $\tilde{\varepsilon}_1$ (red lines) as functions of the drive amplitude ε, calculated using the ideal-case approximation, Eqs. (3.4) and (3.5) (dashed straight lines), the third-order formulas (3.27) and (3.30) (solid lines without symbols), and numerically (solid lines with symbols). We used the qubit-qubit coupling $g/2\pi = 3$ MHz, qubit anharmonicity $\eta_c/2\pi = \eta_t/2\pi = 300$ MHz, and detuning $\Delta/2\pi = 130$ MHz.

this formula $E_{10} = \Delta + \delta$, $E_{21} = \Delta + \delta - \eta_c$, $E_{31} = 2(\Delta + \delta) - 3\eta_c$, and we can neglect δ (i.e., $\delta = 0$). For a complex ε, we need to replace ε^2 in parentheses with $|\varepsilon|^2$.

Figure 3.1 shows the effective drive amplitudes $\tilde{\varepsilon}_0$ and $\tilde{\varepsilon}_1$ as functions of the actual drive amplitude ε calculated in several ways for the following parameters (which are some typical experimental parameters): $g/2\pi = 3$ MHz, $\eta_c/2\pi = 300$ MHz, $\Delta/2\pi = 130$ MHz. The blue lines (initially going down) show $\tilde{\varepsilon}_0$, the orange lines (initially going up) show $\tilde{\varepsilon}_1$. The solid lines without symbols are calculated using Eqs. (3.27) and (3.30) (using $\delta = 0$), while the straight dashed lines represent the simple linear approximation, Eqs. (3.4) and (3.5). The solid lines with symbols show the numerical results [the numerical procedure is

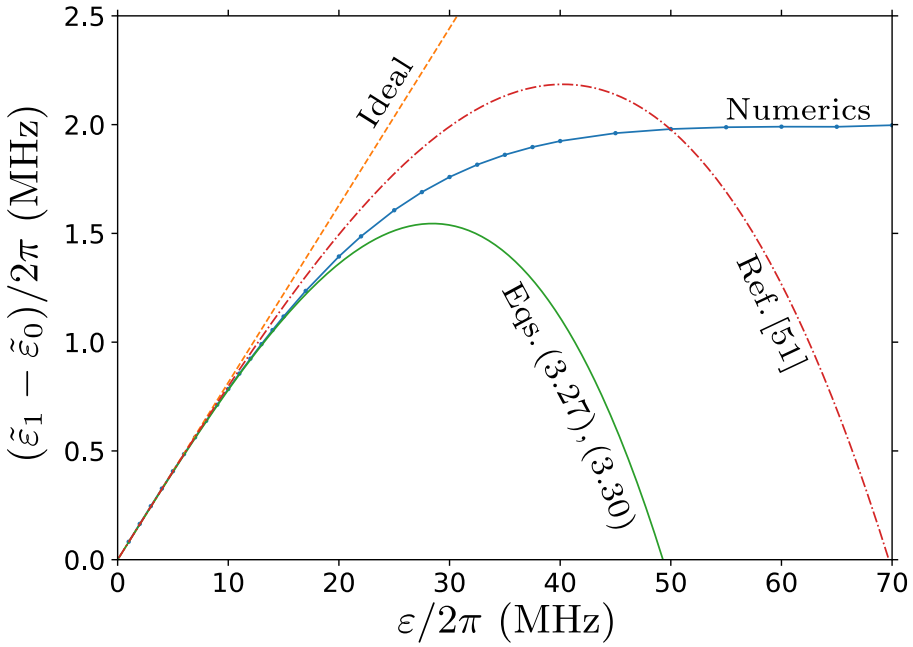

Figure 3.2: The CR gate speed $\tilde{\varepsilon}_1 - \tilde{\varepsilon}_0$ as a function of the drive amplitude ε, calculated using the linear-order approximation (3.8) (dashed straight line), third-order approximations (3.27) and (3.30) (green solid line), Eq. (4.25) of Ref. [51] (dash-dotted red line), and numerically (blue solid line with symbols). The parameters are the same as in Fig. 3.1.

described later in Chapter 4, for numerics we assume $\eta_t = \eta_c$ and $\omega_d = \omega_t^{c0}$].

We see that the third-order approximation [Eqs. (3.27) and (3.30)] correctly describes deviation of the dependences $\tilde{\varepsilon}_0(\varepsilon)$ and $\tilde{\varepsilon}_1(\varepsilon)$ from the ideal straight lines at relatively small ε, but fails to fit well the case of relatively large ε. This is because higher-order terms become important even for moderate values of ε. The problem has similarity with a poor performance of the perturbation approach in analysis of the circuit QED measurement of transmons for the photon number n_{ph} comparable to the critical number n_{crit} [59]. The correspondence between the two problems is $n_{ph}/n_{crit} \leftrightarrow (2\varepsilon/\Delta)^2$.

Figure 3.2 shows the difference $\tilde{\varepsilon}_1 - \tilde{\varepsilon}_0$ as a function of ε (for the same parameters as in Fig. 3.1), also calculated in several ways. The dashed straight line corresponds to the

simple formula (3.8) for the ideal operation. The numerical results are shown by the blue solid line with symbols. The green solid line is calculated using Eqs. (3.27) and (3.30). The red dash-dotted line is calculated using Eq. (4.25) of Ref. [51] (and also the equation in Appendix C of Ref. [51]), which differs from our result by the twice smaller coefficient for the term proportional to ε^3. By comparing the red line with the blue line at relatively small ε (where the third-order approximation is supposed to work), we see that the analytical result of Ref. [51] contradicts our numerical results. In contrast, our analytical result (green line) fits well our numerics for small ε. Possibly there are misprints in Ref. [51].

3.3 Semi-analytical results

The method developed in the previous section can be naturally extended to arbitrary large drive amplitudes ε. For that the eigenstates $\overline{|n\rangle_\varepsilon}$ of the control-qubit Hamiltonian (3.16) can be found numerically, and then the effective drive amplitudes $\tilde{\varepsilon}_n$ can be calculated using Eq. (3.18). Since numerical diagonalization of a Hamiltonian for few levels is very easy (compared with full numerical simulation of the two-qubit evolution discussed in the next chapter), we call this method semi-analytical.

Figure 3.3 shows comparison of the semi-analytical results (dashed lines) for $\tilde{\varepsilon}_0$ and $\tilde{\varepsilon}_1$ with the numerical results (solid lines with symbols, numerical procedure is discussed in Chapter 4). The parameters are the same as in Figs. 3.1 and 3.2, except we use two values of the detuning: $\Delta/2\pi = 130$ MHz and 190 MHz. We see that the numerical results agree with semi-analytics very well for all values of the drive amplitude ε (the lines are practically indistinguishable). We found a similar very good agreement for other values of

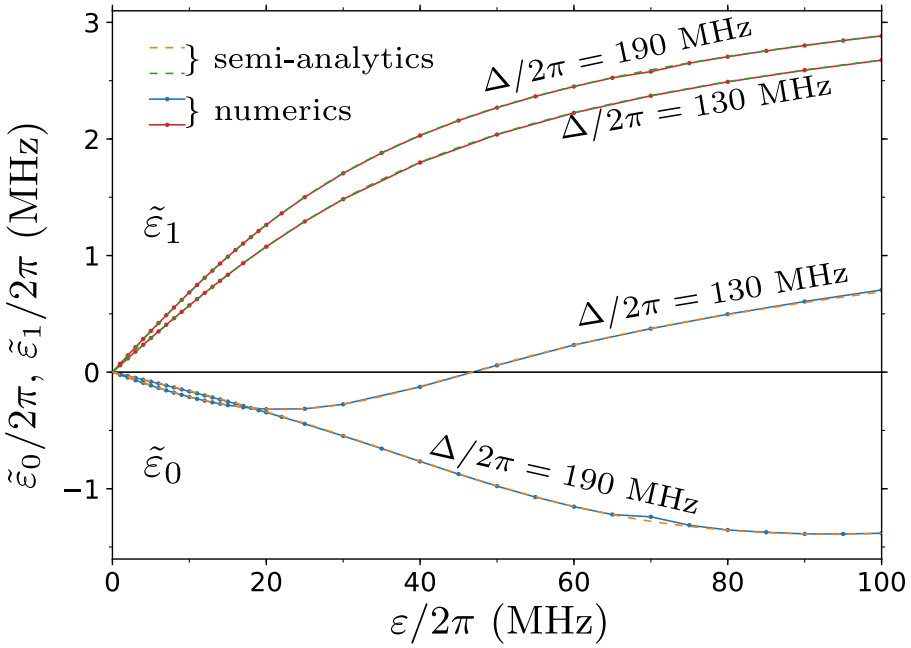

Figure 3.3: Effective drive amplitudes $\tilde{\varepsilon}_0$ and $\tilde{\varepsilon}_1$ as functions of ε, calculated numerically (solid lines with symbols) and using the semi-analytical approach, Eqs. (3.15)–(3.18) (dashed lines, practically coinciding with the solid lines). We used $g/2\pi = 3$ MHz, $\eta_c/2\pi = \eta_t/2\pi = 300$ MHz, and two values for the detuning: $\Delta/2\pi = 130$ MHz and 190 MHz.

the parameters as well. Therefore, the semi-analytical method based on Eqs. (3.15)–(3.18) seems to be a sufficiently simple and accurate way of analyzing the dependence of the CR gate speed on parameters.

Note that $\tilde{\varepsilon}_n$ in the semi-analytical method is proportional to the qubit-qubit coupling g and also depends on two dimensionless ratios: Δ/η_c and ε/η_c (assuming $\delta = 0$). In the Duffing (Kerr) approximation (2.4), these two ratios fully define the eigenstates (3.17) (in a better approximation [57,58] the results will also depend on the dimensionless parameter η_c/ω_c). Therefore, in our analysis the ratio $\tilde{\varepsilon}_n/g$ is a function of *only two parameters*: Δ/η_c and ε/η_c.

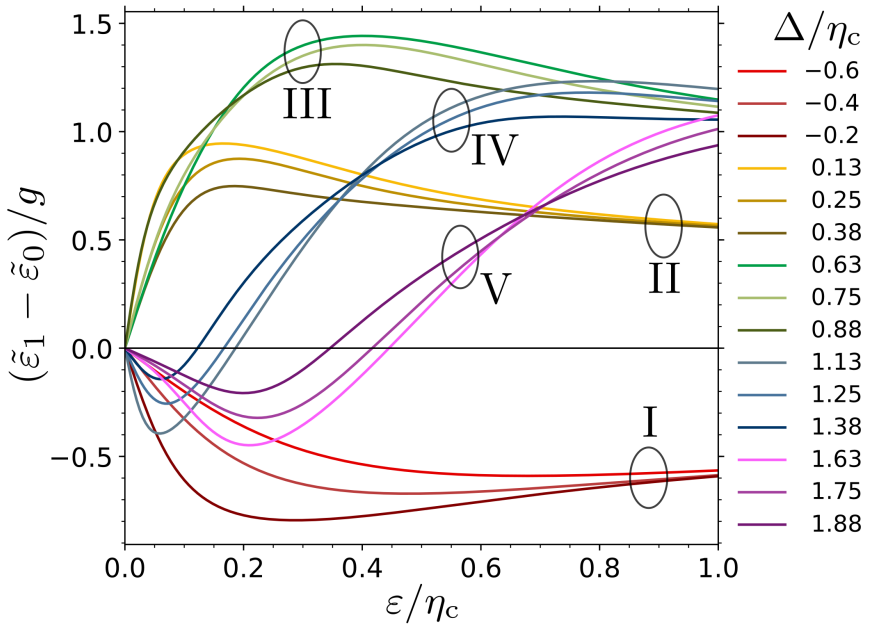

Figure 3.4: Dimensionless CR gate speed $(\tilde{\varepsilon}_1 - \tilde{\varepsilon}_0)/g$ as a function of the dimensionless drive amplitude ε/η_c for several values of the dimensionless detuning Δ/η_c. The lines are calculated using the semi-analytical method (3.15)–(3.18). At large ε, the lines group into "bands". The group I is for $\Delta/\eta_c < 0$, the group II is for Δ/η_c in the interval $(0, 1/2)$. Similarly, the groups III, IV and V are for Δ/η_c in the intervals $(1/2, 1)$, $(1, 3/2)$, and $(3/2, 2)$, respectively.

Figure 3.4 shows the dimensionless speed $(\tilde{\varepsilon}_1 - \tilde{\varepsilon}_0)/g$ of the CR gate as a function of the dimensionless drive amplitude ε/η_c for several values of the dimensionless detuning Δ/η_c. While the behavior at small ε agrees with Eq. (3.8) (not shown), the behavior at large ε mostly depends on whether the detuning $\Delta = \omega_c - \omega_t$ is negative or positive and on the integer part of the ratio $2\Delta/\eta_c$ for positive Δ. As seen in Fig. 3.4, at large ε the lines group according to the interval to which Δ belongs: $(-\infty, 0)$, $(0, \eta_c/2)$, $(\eta_c/2, \eta_c)$, $(\eta_c, 3\eta_c/2)$, $(3\eta_c/2, 2\eta_c)$, etc. (in Fig. 3.4 these groups of lines are labeled sequentially as I, II, III, etc.). We do not show the lines for $\Delta/\eta_c = 0$, 1/2, 1, 3/2, etc. because at these values there is a resonance between the levels, $E_n^{(c)} = E_0^{(c)}$ and $E_{n-1}^{(c)} = E_1^{(c)}$ for $n = 2\Delta/\eta_c + 1$

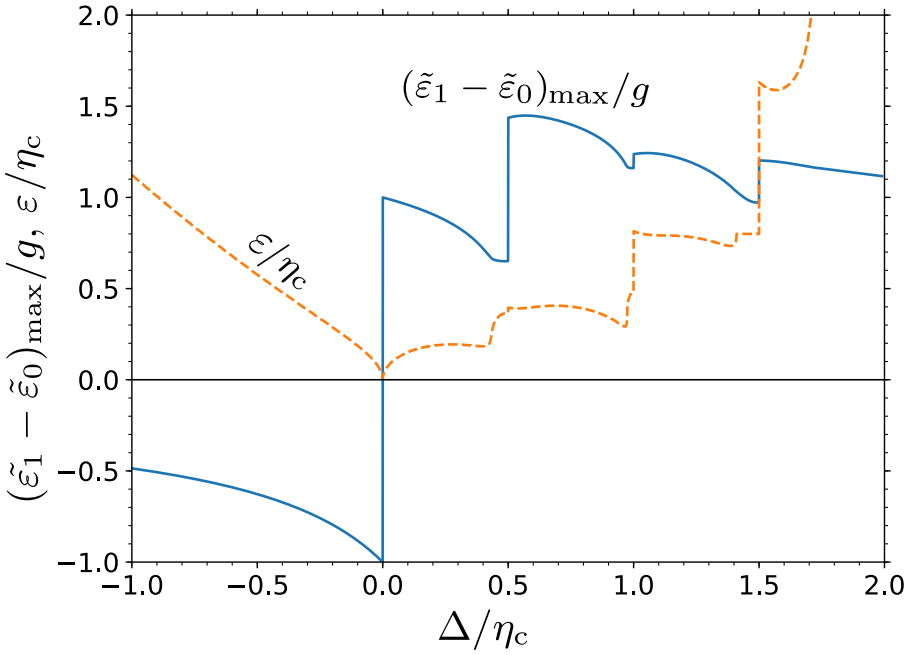

Figure 3.5: Maximized (minimized for negative values) dimensionless speed $(\tilde{\varepsilon}_1 - \tilde{\varepsilon}_0)_{\max}/g$ (solid blue line) and corresponding dimensionless drive amplitude ε/η_c (dashed orange line) as functions of the dimensionless detuning Δ/η_c. The lines are calculated using the semi-analytical method (3.15)–(3.18).

[see Eq. (2.4) for $\delta = 0$], and correspondingly the CR gate does not operate as intended (due to a very large leakage – see below), also leading to computational problems in the semi-analytical and numerical calculations.

It is simple to understand why the lines in Fig. 3.4 group into "bands" at large ε. In the solution of the Schrödinger equation (3.15) for the Hamiltonian (3.16) at large ε, the main effect is a strong level repulsion, which depends on the relative position (topology) of the bare energy levels $E_n^{(c)}$ (i.e., which level is in between which levels; the topology does not change with ε because of the adiabatic theorem); however, the level repulsion does not depend much on the values of the initial bare level difference (since ε dominates). This is why there is a grouping of lines in Fig. 3.4.

We see that most of the lines in Fig. 3.4 (all the lines in the experimentally important groups II and III) have a maximum, with a relatively minor decrease after it (experimental results [40, 47] are somewhat similar). Experimentally, faster speed $(\tilde{\varepsilon}_1 - \tilde{\varepsilon}_0)$ means shorter CNOT gate duration and there is no benefit to increase the drive amplitude beyond the maximum in Fig. 3.4.

The solid blue line in Fig. 3.5 shows the maximum value $(\tilde{\varepsilon}_1 - \tilde{\varepsilon}_0)_{\max}/g$ of the dimensionless speed (or the minimum value for the negative speed) as a function of the dimensionless detuning Δ/η_c. The dimensionless drive amplitude ε/η_c at which this maximum is reached, is shown by the dashed orange line. We see that the maximum CR gate speed is reached for the detuning Δ between $\eta_c/2$ and η_c (group III in Fig. 3.4). Note that our semi-analytical approach cannot be applied in close vicinities of the detinings $\Delta/\eta_c = 0$, 0.5, 1, 1.5, etc. The dependence of $(\tilde{\varepsilon}_1 - \tilde{\varepsilon}_0)_{\max}$ on Δ was measured experimentally [47] and it showed a crudely similar behavior.

Chapter 4

Numerical approach

Numerically, we simulate the quantum evolution due to the rotating-frame Hamiltonian (2.1)–(2.8), taking into account 7 levels in the control qubit and 5 levels in the target qubit, so that there are 35 levels in total. The simulation is based on matrix exponentiation for a time-dependent Hamiltonian, using the second-order Magnus expansion [56]. We also tried to use the fourth-order Runge-Kutta method, but found that for our typical parameters it is almost an order of magnitude slower to reach the same desired accuracy.

We start with diagonalization of the time-independent part $H_{\rm qb}+H_g$ of the Hamiltonian, and then the whole simulation is done in the eigenbasis $\overline{|n,m\rangle}$ of $H_{\rm qb}+H_g$, with the time-dependent drive Hamiltonian $H_\varepsilon(t)$ (expended in the eigenbasis) causing the evolution. In this way we obtain a 35×35 unitary evolution matrix V (in the eigenbasis $\overline{|n,m\rangle}$) for a given pulse of the drive amplitude $\varepsilon(t)$ with duration $\tau_{\rm p}$ (the pulse shape is discussed later). The matrix V is then projected onto the computational two-qubit subspace, thus producing a 4×4 matrix M, which is no longer unitary (here projection means the simple elimination

of all other elements). Note that the reduced matrix M is still defined in the eigenbasis, consisting of states $\overline{|0,0\rangle} = |0,0\rangle$, $\overline{|0,1\rangle}$, $\overline{|1,0\rangle}$ and $\overline{|1,1\rangle}$.

To find *fidelity* of an operation, we compare the reduced matrix M with the desired 4×4 unitary operation, which we denote U. The fidelity between M and U is defined as [60, 61]

$$F_{MU} = \frac{\mathrm{Tr}(M^\dagger M)}{d(d+1)} + \frac{|\mathrm{Tr}(M^\dagger U)|^2}{d(d+1)}, \tag{4.1}$$

where $d = 4$ is the dimension of the two-qubit Hilbert space. This definition of the gate fidelity is equal to the final-state fidelity (squared overlap) averaged over all (pure) initial states in the two-qubit subspace; therefore, F_{MU} corresponds to the fidelity in Randomized Benchmarking (assuming that the states leaked outside the computational subspace never come back).

Even though the final goal of the CR gate operation is to produce CNOT (after additional single-qubit rotations), in the numerical procedure the desired U is obviously not the CNOT. Instead, for a given pulse $\varepsilon(t)$ (which produces some matrix V and corresponding matrix M), we *define U as the closest two-qubit unitary* (i.e., which maximizes the fidelity F_{MU}), restricted to the following class:

$$U = e^{i\theta_0}|0\rangle\langle 0|_{\mathrm{c}}\, e^{-i(\varphi_0/2)X_{\mathrm{t}}} + e^{i\theta_1}|1\rangle\langle 1|_{\mathrm{c}}\, e^{-i(\varphi_1/2)X_{\mathrm{t}}}, \tag{4.2}$$

where $|n\rangle\langle n|_{\mathrm{c}}$ acts on the control qubit, while X_{t} acts on the target qubit (as mentioned above, we use the eigenbasis of $H_{\mathrm{qb}} + H_g$ for both M and U). The condition (4.2) means that the state of the control qubit does not change (in the eigenbasis). Also, for state $|0\rangle$ of the control qubit, the target qubit is rotated about x axis over angle φ_0; similarly, for

control-qubit state $|1\rangle$, the target qubit is rotated about x axis over angle φ_1. Besides that, in Eq. (4.2) there are phases θ_0 and θ_1; disregarding the unimportant overall phase, this can be interpreted as z-rotation of the control qubit over angle $\theta_1 - \theta_0$. Without loss of generality, we can assume $\theta_0 = 0$ (while keeping the same $\theta_1 - \theta_0$) since this affects only the overall phase, and the definition (4.1) of the fidelity F_{MU} is insensitive to the overall phase of U. Note that Eqs. (4.1) and (4.2) can be easily generalized to include the third state of the control qubit (to consider it as a qutrit); however, here we consider only the two-level subspace.

Thus, to find U for a given pulse of $\varepsilon(t)$, we maximize F_{MU} over parameters φ_0, φ_1, and $\theta_1 - \theta_0$. Fortunately, these optimal angles are given by analytical formulas in terms of the matrix elements of M:

$$\varphi_0 = -\arg\left(\frac{M_{11} + M_{22} + M_{12} + M_{21}}{M_{11} + M_{22} - M_{12} - M_{21}}\right), \tag{4.3}$$

$$\varphi_1 = -\arg\left(\frac{M_{33} + M_{44} + M_{34} + M_{43}}{M_{33} + M_{44} - M_{34} - M_{43}}\right), \tag{4.4}$$

$$\theta_0 = \arg[(M_{11} + M_{22})\cos(\varphi_0/2) + i(M_{12} + M_{21})\sin(\varphi_0/2)], \tag{4.5}$$

$$\theta_1 = \arg[(M_{33} + M_{44})\cos(\varphi_1/2) + i(M_{34} + M_{43})\sin(\varphi_1/2)], \tag{4.6}$$

where the rows (and columns) 1, 2, 3, and 4 of the matrix M correspond to the states $\overline{|00\rangle}$, $\overline{|01\rangle}$, $\overline{|10\rangle}$, and $\overline{|11\rangle}$, respectively. In this way, for a given pulse $\varepsilon(t)$, the CR gate operation is characterized by 4 resulting parameters: the angles φ_0, φ_1, and $\theta_0 - \theta_1$ of the unitary (4.2) and also infidelity $1 - F_{MU}$, which is due to leakage outside of the computational two-qubit subspace and also due to the computational-space unitary not fitting well the class (4.2).

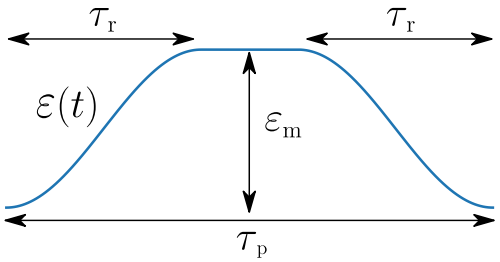

Figure 4.1: Pulse shape $\varepsilon(t)$ used in numerical simulations. The total pulse duration is τ_p, each cosine-shaped ramp has duration τ_r, the drive amplitude in the middle flat part is ε_m.

We consider the pulse shape $\varepsilon(t)$ of duration τ_p,

$$\varepsilon(t) = \begin{cases} \dfrac{1-\cos(\pi t/\tau_r)}{2}\,\varepsilon_m, & 0 \le t \le \tau_r, \\ \varepsilon_m, & \tau_r \le t \le \tau_p - \tau_r, \\ \dfrac{1-\cos[\pi(\tau_p - t)/\tau_r]}{2}\,\varepsilon_m, & \tau_p - \tau_r \le t \le \tau_p, \end{cases} \tag{4.7}$$

which consists of the flat middle part with the *real* amplitude ε_m of the drive and two symmetric cosine-shaped ramps (so that there are no kinks), each with duration τ_r – see Fig. 4.1. As discussed later, sufficiently long ramps are needed to reduce leakage outside of the computational subspace.

Effective drive amplitudes $\tilde{\varepsilon}_0$ and $\tilde{\varepsilon}_1$ used in Chapter 3 (Figs. 3.1–3.3) have been numerically calculated as the derivatives,

$$\tilde{\varepsilon}_0 = \frac{1}{2}\frac{\partial\varphi_0}{\partial\tau_p}, \quad \tilde{\varepsilon}_1 = \frac{1}{2}\frac{\partial\varphi_1}{\partial\tau_p}, \tag{4.8}$$

while keeping the ramp duration τ_r, the middle-part amplitude ε_m (which replaces ε in Chapter 3), and other parameters fixed.

The small drive frequency detuning δ in numerical simulations is chosen in the following way. We first use the laboratory frame, i.e., $\delta = \omega_t$ (for the Duffing oscillator model we can also use $\delta = \omega_t = 0$) and calculate the eigenfrequencies of the target qubit

$\omega_{\rm t}^{\rm c0}$ and $\omega_{\rm t}^{\rm c1}$ – see Eq. (2.9). If we want the drive to be exactly on resonance with the target qubit when the control qubit is $|0\rangle$, then we need to use $\omega_{\rm d} = \omega_{\rm t}^{\rm c0}$, which gives $\delta = \omega_{\rm t} - \omega_{\rm t}^{\rm c0}$. Similarly, if we want $\omega_{\rm d} = \omega_{\rm t}^{\rm c1}$ (the drive on resonance with the target qubit when the control qubit is $|1\rangle$), then we use $\delta = \omega_{\rm t} - \omega_{\rm t}^{\rm c1}$. If we want the drive frequency exactly in between the two resonances, $\omega_{\rm d} = (\omega_{\rm t}^{\rm c0} + \omega_{\rm t}^{\rm c1})/2$, then we use $\delta = \omega_{\rm t} - (\omega_{\rm t}^{\rm c0} + \omega_{\rm t}^{\rm c1})/2$. Note that the frequency differences $\omega_{\rm t} - \omega_{\rm t}^{\rm c0}$ and $\omega_{\rm t} - \omega_{\rm t}^{\rm c1}$ do not depend on a choice of the rotating frame.

Since experimentally the CR gate is mainly used to realize CNOT, in the numerical simulations we are mostly interested in the operations equivalent to CNOT up to single-qubit rotations. In analyzing the CNOT-equivalent gates, we usually use the pulse shape, in which the ramps occupy 30% of the whole pulse duration each, i.e., $\tau_{\rm r} = 0.3\,\tau_{\rm p}$ in Eq. (4.7) (Fig. 7.4 is an exception). For a given middle-part amplitude $\varepsilon_{\rm m}$, we find the shortest pulse duration $\tau_{\rm p}$, for which

$$\varphi_1 - \varphi_0 = \pi \pmod{2\pi}. \tag{4.9}$$

This is what we call the CNOT gate duration $\tau_{\rm p}^{\rm CNOT}(\varepsilon_{\rm m})$, neglecting durations of the additional single-qubit operations (x-rotation of the target qubit and z-rotation of the control qubit). We assume perfect fidelity of single-qubit operations; therefore, the CNOT infidelity is $1 - F_{MU}$ for the pulse with duration $\tau_{\rm p}^{\rm CNOT}(\varepsilon_{\rm m})$.

In the simulations we fully neglect decoherence. A crude estimate of the fidelity decrease ΔF due to energy relaxation and pure dephasing can be obtained by considering idle qubits (averaged over pure states), which decohere during time $\tau_{\rm p}^{\rm CNOT}$. This gives the

estimate

$$\Delta F \simeq \frac{4}{10}\,\frac{\tau_{\rm p}^{\rm CNOT}}{T_1} + \frac{4}{5}\,\frac{\tau_{\rm p}^{\rm CNOT}}{T_2}, \tag{4.10}$$

where T_1 is the energy relaxation time and T_2 is the dephasing time (which includes contribution due to energy relaxation). Note, however, that actual fidelity decrease ΔF can be significantly larger than this estimate because the CR gate operation involves significant population of the level $|2\rangle$ and even higher levels of the control qubit, which have poorer coherence than the level $|1\rangle$.

One run of the evolution simulation for a given pulse duration typically takes a few seconds on a desktop or a laptop computer. Finding $\tau_{\rm p}^{\rm CNOT}$ requires several tens of runs, so a typical time to produce a line showing dependence of the CNOT gate operation on $\varepsilon_{\rm m}$ is few hours. The simulation time significantly depends on the number of time steps in the pulse ramps; we have used 600 time steps for each ramp, which gives a quite good accuracy of the simulations. For quick (and much less accurate) simulations it is possible to use $\sim$100 time steps per ramp.

Chapter 5

Numerical CNOT gate duration and single-qubit rotations

5.1 CNOT gate duration

In numerical simulations we use the qubit-qubit coupling $g/2\pi = 3$ MHz (except in Fig. 7.3) and transmon anharmonicity $\eta_c/2\pi = \eta_t/2\pi = 300$ MHz. Figure 5.1 shows the CNOT gate duration $\tau_p^{\rm CNOT}$ as a function of the drive amplitude ε_m in the middle part of a pulse (with $\tau_r = 0.3\,\tau_p$), for several values of the qubit-qubit detuning $\Delta/2\pi$: -70, 70, 130, and 190 MHz. For numerical results (solid lines) we choose $\omega_d = \omega_t^{c0}$, i.e., $\delta = \omega_t - \omega_t^{c0}$. The dashed lines (almost coinciding with the solid lines) show the result of the semi-analytical method, in which we use Eq. (3.2) and integrate over the pulse shape. We see that the semi-analytical method works very well; however, there are (barely) visible deviations at both small and large amplitudes ε_m. We guess the slight deviation at large ε_m is because for

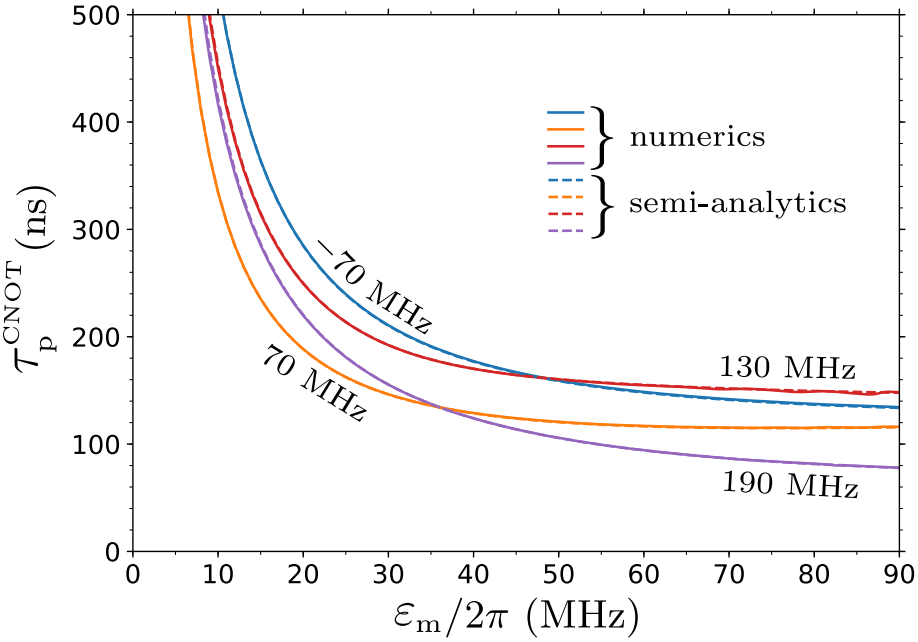

Figure 5.1: CNOT gate duration $\tau_{\rm p}^{\rm CNOT}$ (neglecting single-qubit rotations) as a function of the mid-pulse drive amplitude $\varepsilon_{\rm m}$ for several detunings: $\Delta/2\pi = -70$, 70, 130, and 190 MHz, while $g/2\pi = 3$ MHz and $\eta_{\rm c}/2\pi = \eta_{\rm t}/2\pi = 300$ MHz. Solid lines are calculated numerically, dashed lines (almost coinciding with the solid lines) are calculated using the semi-analytical method.

a short pulse, the non-adiabatic evolution during the ramps starts to play a noticeable role. The deviation at small $\varepsilon_{\rm m}$ is because here the zz-coupling (2.10) starts to play a relatively significant role.

For a more detailed analysis of the deviation at small $\varepsilon_{\rm m}$, solid lines in Fig. 5.2 show the numerical CNOT time $\tau_{\rm p}^{\rm CNOT}$ for $\Delta/2\pi = 130$ MHz and three values of the drive frequency: $\omega_{\rm d} = \omega_{\rm t}^{\rm c0}$ (blue line, drive on resonance with the target qubit when the control qubit is $|0\rangle$, i.e., $\delta = \omega_{\rm t} - \omega_{\rm t}^{\rm c0}$), $\omega_{\rm d} = \omega_{\rm t}^{\rm c1}$ (orange line, on resonance when the control qubit is $|1\rangle$, i.e., $\delta = \omega_{\rm t} - \omega_{\rm t}^{\rm c1}$), and exactly in between, $\omega_{\rm d} = (\omega_{\rm t}^{\rm c0} + \omega_{\rm t}^{\rm c1})/2$ (green line). The dashed line shows the semi-analytical result (actually, there are three dashed lines for the

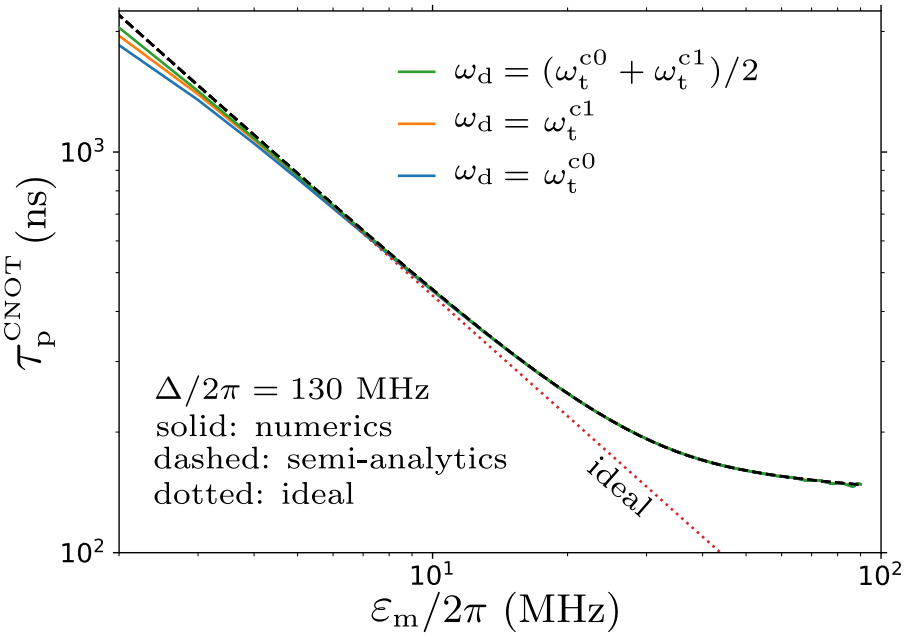

Figure 5.2: Solid lines: dependence of the CNOT duration $\tau_{\rm p}^{\rm CNOT}$ on $\varepsilon_{\rm m}$ for three drive frequencies: $\omega_{\rm d} = \omega_{\rm t}^{\rm c0}$ (exact resonance for the control-qubit state $|0\rangle$, blue line), $\omega_{\rm d} = \omega_{\rm t}^{\rm c1}$ (resonance for the control-qubit state $|1\rangle$, orange line), and $\omega_{\rm d} = (\omega_{\rm t}^{\rm c0} + \omega_{\rm t}^{\rm c1})/2$ (exactly in between, green line). Dashed line shows the semi-analytical results, straight dotted line corresponds to Eq. (5.1). We use $\Delta/2\pi = 130$ MHz, other parameters are as in Fig. 5.1.

three values of δ, but they are indistinguishable), and the dotted line shows the ideal result,

$$\tau_{\rm p,\,ideal}^{\rm CNOT} = \frac{\pi/2}{0.7\,\varepsilon_{\rm m}}\,\frac{\Delta(\eta_{\rm c} - \Delta)}{2g\eta_{\rm c}}, \tag{5.1}$$

which follows from Eqs. (3.2) and (3.8) after integration over the pulse shape (4.7) with $\tau_{\rm r}/\tau_{\rm p} = 0.3$ (this integration gives the factor 0.7). We see that the solid lines noticeably deviate down from the dashed line for $\varepsilon_{\rm m}/2\pi$ less than $\sim$5 MHz, with the largest deviation for $\delta = \omega_{\rm t} - \omega_{\rm t}^{\rm c0}$ (blue line). Note that for $\varepsilon/2\pi = 5$ MHz, Eq. (3.8) gives $(\tilde{\varepsilon}_1 - \tilde{\varepsilon}_0)/2\pi = 0.41$ MHz, while $\omega_{zz}/2\pi = 0.15$ MHz [see Eq. (2.11)], so the effect of zz-coupling is expected to be significant.

In particular, for $\omega_{\rm d} = \omega_{\rm t}^{\rm c0}$ (blue line in Fig. 5.2) the drive is exactly on resonance with the target qubit for the control-qubit state $|0\rangle$ and therefore the approximation $\varphi_0 = 0.7\,\tau_{\rm p}^{\rm CNOT} \times 2\tilde{\varepsilon}_0(\varepsilon_{\rm m})$ using Eq. (3.4) should work well (as numerics confirms). In contrast, for the control-qubit state $|1\rangle$, the drive is detuned by ω_{zz} from the target-qubit frequency, which leads to Rabi oscillations with frequency $\sqrt{(2\tilde{\varepsilon}_1)^2 + \omega_{zz}^2}$ within the plane tilted by angle $\mathrm{atan}(\omega_{zz}/2\tilde{\varepsilon}_1)$ from the zy plane (the frequency and the plane are changing in time because of the pulse shape). The larger Rabi frequency (due to ω_{zz} contribution) leads to a shorter CNOT duration than expected analytically, explaining the behavior of solid lines in Fig. 5.2 at small $\varepsilon_{\rm m}$. The same effect (rotation within a tilted plane) leads to a significant infidelity of the CNOT gate at small $\varepsilon_{\rm m}$ – see Chapter 6.

5.2 Single-qubit rotations

As discussed above, in order to realize the CNOT gate, the CR operation with the pulse duration $\tau_{\rm p}^{\rm CNOT}$ should be complemented by single-qubit rotations. The target qubit should be rotated about x-axis over the angle $-\varphi_0$ to compensate the operator $e^{-i(\varphi_0/2)X_{\rm t}}$ in Eq. (4.2). Similarly, the control qubit should be rotated about z-axis to compensate the relative phase $\theta_1 - \theta_0$ and the negative imaginary unit due to the relation $e^{-i(\pi/2)X_{\rm t}} = -iX_{\rm t}$. So, naively we would expect that z-rotation over the angle $\pi/2 - (\theta_1 - \theta_0)$ is needed. However, the angle $\theta_1 - \theta_0$ is numerically computed in the rotating frame of the drive, while experimental z-rotation should be in the rotating frame of the control qubit. Using such rotating frame based on frequency $\omega_{\rm c}^{\rm t0} = E_{|1,0\rangle}^{(\rm lf)} - E_{|0,0\rangle}^{\rm lf}$ (i.e., when the target qubit is $|0\rangle$, as

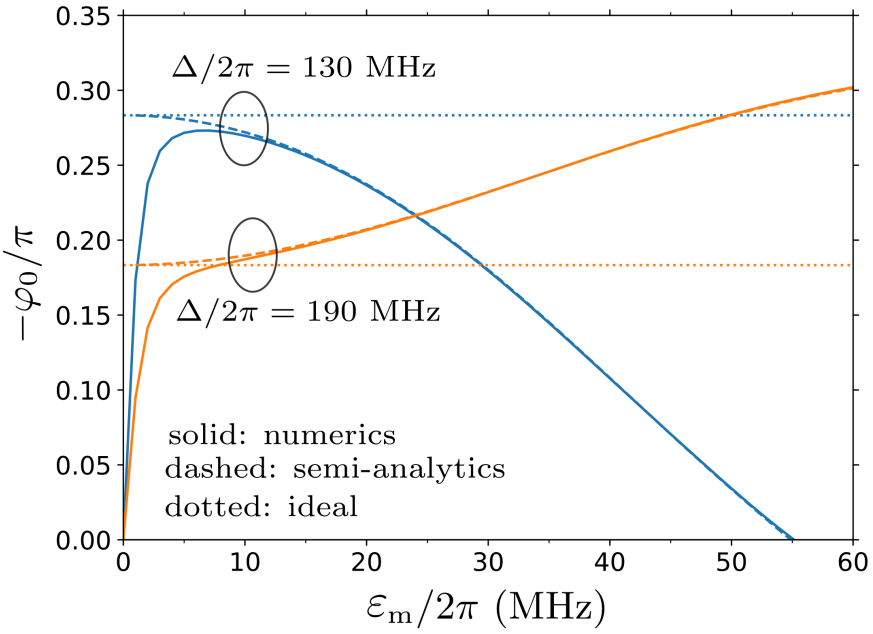

Figure 5.3: The angle $-\varphi_0$ of the compensating target-qubit x-rotation to produce CNOT, as a function of the mid-pulse drive amplitude ε_m. Numerical results are shown by solid lines, semi-analytics is represented by dashed lines, and dotted lines show the ideal result: $-\varphi_0/\pi = (\eta_c - \Delta)/2\eta_c$. Here we use $\Delta/2\pi = 130$ and 190 MHz, $\omega_d = \omega_t^{c0}$, $g/2\pi = 3$ MHz, $\eta_c/2\pi = \eta_t/2\pi = 300$ MHz, and $\tau_r/\tau_p = 0.3$.

usually done in experiments), we need to replace the phase difference $\theta_1 - \theta_0$ with

$$\theta_1' - \theta_0' = \theta_1 - \theta_0 + (\Delta + \delta + \omega_c^{t0} - \omega_c)\,\tau_p^{CNOT}, \tag{5.2}$$

so in an experiment the control qubit should be z-rotated over the angle $\theta_0' - \theta_1' + \pi/2$.

Figure 5.3 shows the angle $-\varphi_0$ (normalized by π) as a function of ε_m for two values of the detuning: $\Delta/2\pi = 130$ and 190 MHz (we use $\omega_d = \omega_t^{c0}$). Solid lines show the numerical results, dashed lines show the corresponding semi-analytical results, and horizontal dotted lines show the ideal result based on Eqs. (3.4) and (3.5): $-\varphi_0 = \pi(\eta_c - \Delta)/2\eta_c$. We see that this ideal result for $-\varphi_0$ is never applicable. The deviation from it at large ε_m is described well by the semi-analytics and is due to the deviations from the ideal

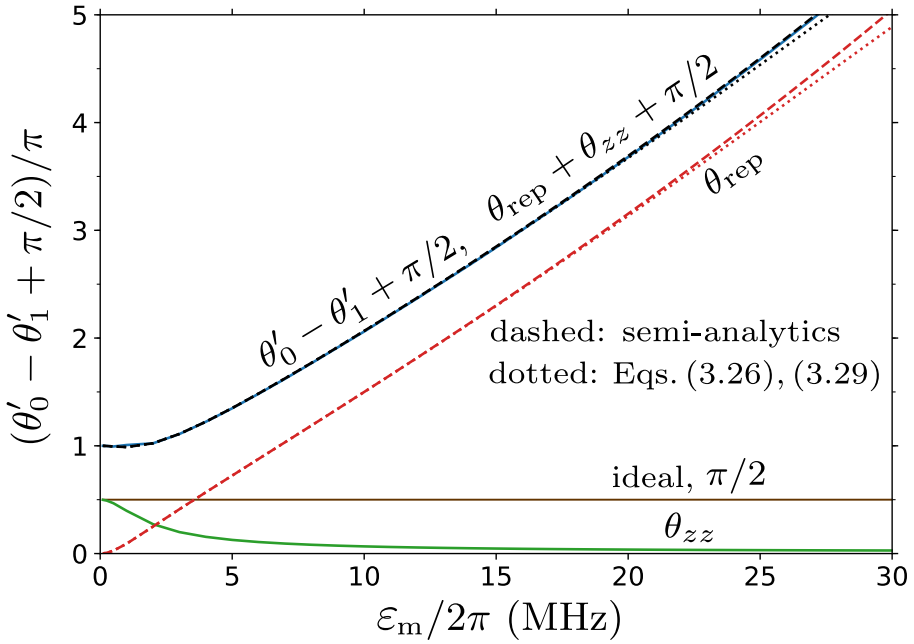

Figure 5.4: Upper (blue) solid line: numerical result for the angle $\theta_0' - \theta_1' + \pi/2$ of z-rotation of the control qubit, needed to produce the CNOT gate. Horizontal (brown) line shows the ideal value $\pi/2$. Dashed and dotted red lines show the contribution $\theta_{\rm rep}$ due to ε-induced level repulsion (5.3), calculated either semi-analytically (dashed line) or via Eqs. (3.26) and (3.29) (dotted line). The lower (green) solid line shows the contribution θ_{zz} given by Eq. (5.4). The upper solid and dashed black lines (very close to the blue solid line) show the sum $\theta_{\rm rep} + \theta_{zz} + \pi/2$. We use $\Delta/2\pi = 130$ MHz and parameters from Fig. 5.3.

straight lines in Fig. 3.3. The deviation from the ideal result in Fig. 5.3 at small $\varepsilon_{\rm m}$ is due to ω_{zz} – the same effect as discussed above for Fig. 5.2.

Upper (blue) solid line in Fig. 5.4 shows the numerical result for the control-qubit rotation angle $\theta_0' - \theta_1' + \pi/2$ (normalized by π) as a function of $\varepsilon_{\rm m}$ for $\Delta/2\pi = 130$ MHz and $\omega_{\rm d} = \omega_{\rm t}^{\rm c0}$. We see that it is quite different from the ideally expected value of $\pi/2$ (horizontal brown line). The difference is mainly due to two effects. First, strong drive $\varepsilon(t)$ causes the level repulsion in the control qubit, which slightly changes the control-qubit frequency and

produces the accumulated angle

$$\theta_{\rm rep} = \int_0^{\tau_{\rm p}} (E_{\overline{|1\rangle}_\varepsilon} - E_{\overline{|0\rangle}_\varepsilon})\, dt. \tag{5.3}$$

(Actually, because the state $|1\rangle$ is assumed to be at the bottom of the Bloch sphere, this produces the z-rotation of $-\theta_{\rm rep}$, so we need to apply the rotation of $+\theta_{\rm rep}$ to compensate it.) The angle $\theta_{\rm rep}$ calculated semi-analytically [see Eq. (3.15)] is shown by the dashed red line in Fig. 5.4; the same angle calculated using analytical results (3.26) and (3.29) is shown by the dotted red line (in both cases we use numerical $\tau_{\rm p}^{\rm CNOT}$ to integrate over the pulse shape). The second contribution into $\theta_0' - \theta_1'$ is due to zz coupling (2.10), which produces

$$\theta_{zz} = \frac{\omega_{zz}}{2}\, \tau_{\rm p}. \tag{5.4}$$

This is because the rotating frame here is based on $\omega_{\rm c}^{\rm t0}$, while $\omega_{\rm c}^{\rm t1} - \omega_{\rm c}^{\rm t0} = \omega_{zz}$ and both states of the target qubit are equivalent. The angle θ_{zz} is shown by the lower (green) solid line in Fig. 5.4. Adding the three contributions, $\theta_{\rm rep} + \theta_{zz} + \pi/2$, we obtain the dashed and dotted black lines (corresponding to the dashed and dotted red lines for $\theta_{\rm rep}$), which are quite close to the numerical result (solid blue line). This confirms the main physical mechanisms contributing to $\theta_0' - \theta_1'$ and also shows that the approximation based on Eqs. (3.26) and (3.29) works quite well.

Chapter 6

Error budget of CR gate

In the previous chapter we have discussed numerical results for the parameters of a CR-based CNOT gate: the duration $\tau_{\rm p}^{\rm CNOT}$ as a function of the mid-pulse drive amplitude $\varepsilon_{\rm m}$ and the compensating single-qubit rotation angles $-\varphi_0$ and $\theta_0' - \theta_1' + \pi/2$. We have seen that these parameters can be obtained quite accurately by the semi-analytical method. In this chapter we discuss numerical results for the infidelity $1 - F_{MU}$ of the CR-based CNOT gate (also as a function of $\varepsilon_{\rm m}$), neglecting decoherence and infidelity of single-qubit rotations (see Chapter 4 for the definition of F_{MU} and the calculation method). These results cannot be obtained semi-analytically and necessarily require full numerical simulations.

6.1 Infidelity of CR gate

Figure 6.1 shows the numerical results for the CNOT gate infidelity $1 - F_{MU}$ as a function of the mid-pulse drive amplitude $\varepsilon_{\rm m}$ for several values of the detuning: $\Delta/2\pi = -70$, 70, 130, and 190 MHz. As in the previous plots, we use $g/2\pi = 3$ MHz, $\eta_{\rm c} = \eta_{\rm t} = 300$ MHz, $\omega_{\rm d} = \omega_{\rm t}^{\rm c0}$, and $\tau_{\rm r} = 0.3\,\tau_{\rm p}$. Most importantly, we see that the infidelity dependence

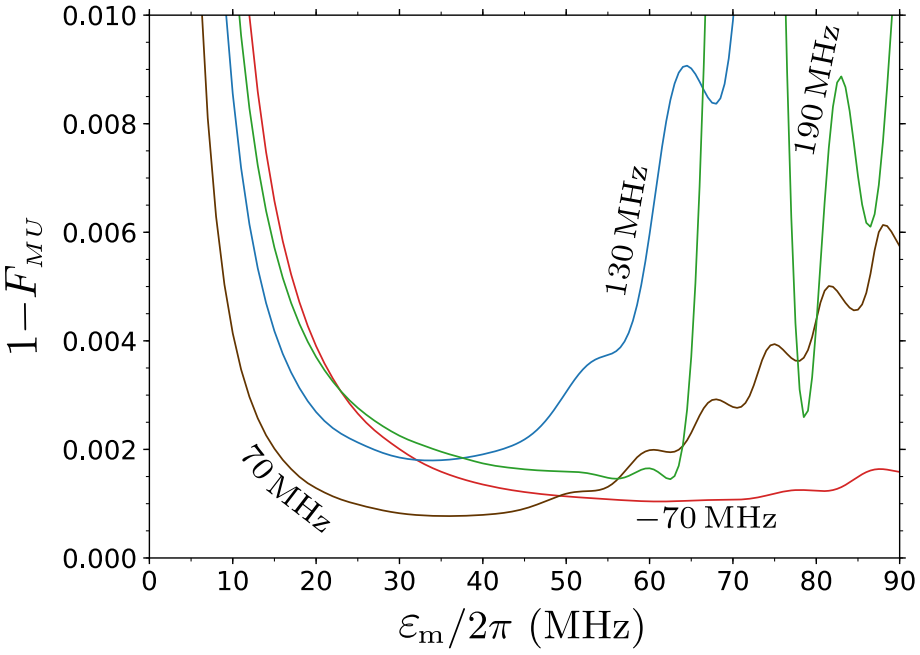

Figure 6.1: Infidelity $1 - F_{MU}$ of the CNOT-equivalent gate as a function of mid-pulse drive amplitude $\varepsilon_{\rm m}$ for several values of the detuning: $\Delta/2\pi = -70$ MHz (red line), 70 MHz (brown line), 130 MHz (blue line), and 190 MHz (green line). Other parameters are $g/2\pi = 3$ MHz, $\eta_{\rm c}/2\pi = \eta_{\rm t}/2\pi = 300$ MHz, $\omega_{\rm d} = \omega_{\rm t}^{\rm c0}$, and $\tau_{\rm r}/\tau_{\rm p} = 0.3$.

on $\varepsilon_{\rm m}$ has a minimum, and at this minimum the infidelity is crudely 10^{-3} for all lines. Second observation is that the minimum is not sharp and is reached for the values of the drive amplitude $\varepsilon_{\rm m}$, above which the CNOT duration $\tau_{\rm p}^{\rm CNOT}$ does not become significantly shorter by a further increase of $\varepsilon_{\rm m}$ (see Figs. 3.4 and 5.1). Note that we do not take into account effect of decoherence, which can be crudely estimated by Eq. (4.10). If decoherence were added, then the minima in Fig. 6.1 would shift to higher values of $\varepsilon_{\rm m}$; however, since the corresponding decrease of $\tau_{\rm p}^{\rm CNOT}$ is not significant, the benefit for fidelity is also not significant; moreover, using higher drive amplitudes could lead to other experimental problems. Therefore, we think the optimum values of $\varepsilon_{\rm m}$ in Fig. 6.1 should be somewhat close to experimental optima.

6.2 Error budget

To understand the reason for the mimima in Fig. 6.1 and to understand the physical mechanisms contributing to the infidelity (error budget), we have done the following more detailed calculations. We remind that we calculate fidelity F_{MU} between the non-unitary 4×4 matrix M (which is the projection of a 35×35 matrix of actual evolution onto the computational subspace) and the closest unitary matrix U, which belongs to the class (4.2) with $\varphi_1 - \varphi_0 = \pi \pmod{2\pi}$ for a CNOT-equivalent gate. Now let us consider a bigger class of unitary matrices and define $\tilde{M}$ as the matrix, which is closest to M out of unitaries satisfying the condition

$$\tilde{M} = |0\rangle\langle 0|_{\rm c}\, \tilde{U}_0^{\rm t} + |1\rangle\langle 1|_{\rm c}\, \tilde{U}_1^{\rm t}, \tag{6.1}$$

where $\tilde{U}_0^{\rm t}$ and $\tilde{U}_1^{\rm t}$ are any 2×2 unitary matrices acting on the target qubit (here "closest" means that $\tilde{M}$ maximizes the fidelity $F_{M\tilde{M}}$). From this definition, $\tilde{M}$ does not change the control-qubit states $|0\rangle$ and $|1\rangle$ (i.e., does not allow any leakage from them), but its rotation of the target qubit is arbitrary. The matrix U [Eq. (4.2)] is more restrictive in the sense that it allows only x-rotations of the target qubit.

To clarify the error budget, we calculate additional infidelities $1 - F_{M\tilde{M}}$ (between M and $\tilde{M}$) and $1 - F_{\tilde{M}U}$ (between $\tilde{M}$ and U) for the CNOT-equivalent CR operations. The idea is that the infidelity $1 - F_{M\tilde{M}}$ is due to leakages (from the control-qubit states $|0\rangle$ and $|1\rangle$ to any state and also outside of the computational subspace for the target qubit). In contrast, the infidelity $1 - F_{\tilde{M}U}$ is due to imperfect unitary rotations of the target qubit. From the physical approach of separation of the error into these different mechanisms, we

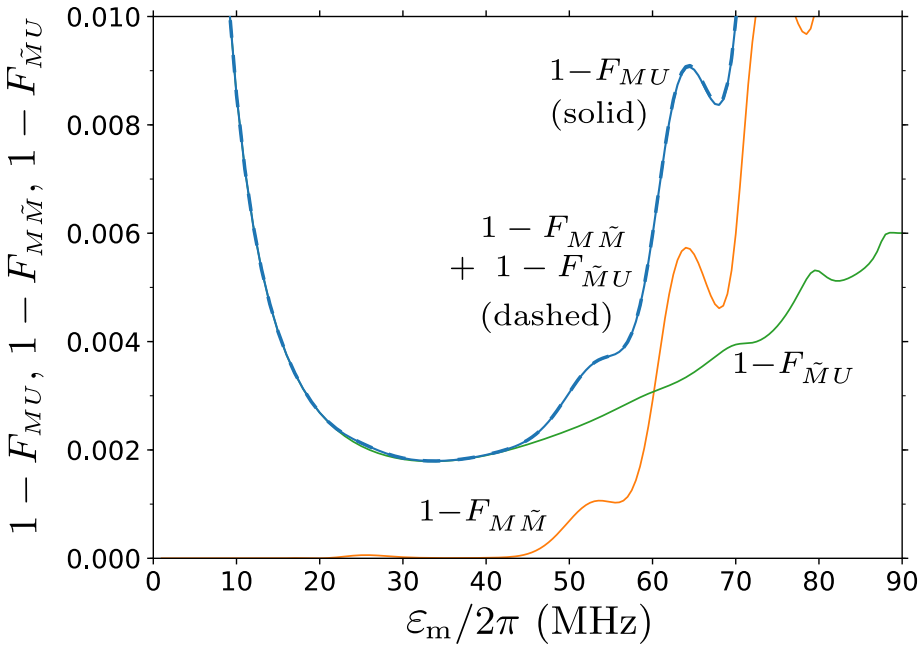

Figure 6.2: Decomposition of the CNOT gate infidelity $1 - F_{MU}$ (blue solid line) into the leakage contribution $1 - F_{M\tilde{M}}$ (orange line) and contribution $1 - F_{\tilde{M}U}$ due to imperfect unitaries (green line). The sum $(1 - F_{M\tilde{M}}) + (1 - F_{\tilde{M}U})$ (dashed blue line) is practically indistinguishable from the solid blue line. We use $\Delta/2\pi = 130$ MHz and parameters from Fig. 6.1.

would expect

$$1 - F_{MU} \approx (1 - F_{M\tilde{M}}) + (1 - F_{\tilde{M}U}). \tag{6.2}$$

This is not an exact relation mathematically (the exact relation would require that certain elements of the quantum process tomography matrix for M have exactly zero real and/or imaginary parts). However, numerical results (e.g., Fig. 6.2) show that this relation is very accurate.

In Fig. 6.2, the blue line is the same as the blue line in Fig. 6.1 ($\Delta/2\pi = 130$ MHz). For the same case, the orange line shows $1 - F_{M\tilde{M}}$, green line shows $1 - F_{\tilde{M}U}$, and the dashed blue line (practically indistinguishable from the solid blue line) shows the

sum $(1 - F_{M\tilde{M}}) + (1 - F_{\tilde{M}U})$. We see that the total infidelity $1 - F_{MU}$ can really be decomposed into the infidelity $1 - F_{M\tilde{M}}$ due to leakages and infidelity $1 - F_{\tilde{M}U}$ due to imperfect untaries acting on the target qubit. Similar decomposition into leakages and imperfect unitaries works also well for other lines in Fig. 6.1 (relative inaccuracy of the decomposition is typically about 10^{-3}).

Besides introducing the error budget via the decomposition (6.2), we also tried a further decomposition by introducing another 4×4 matrix $\tilde{M}'$, which is the closest to M two-qubit unitary. In this case the infidelity $1 - F_{M\tilde{M}'}$ is due to leakages outside of the computational subspace, while the infidelity $1 - F_{\tilde{M}'\tilde{M}}$ is due to unitary transitions between states $|0\rangle$ and $|1\rangle$ of the control qubit (which in our terminology are also leakages for a CR gate). Then the infidelity consists of 3 components,

$$1 - F_{MU} \approx (1 - F_{M\tilde{M}'}) + (1 - F_{\tilde{M}'\tilde{M}}) + (1 - F_{\tilde{M}U}). \tag{6.3}$$

We have checked that this relation is quite accurate numerically. However, for the cases we checked, the matrix $\tilde{M}'$ was very close to either M or $\tilde{M}$ (depending on the detuning Δ, which mostly determines the strongest leakage process). Therefore, usually only two terms in Eq. (6.3) are significant, and this is why below we will continue using the simpler decomposition (6.2).

As seen in Fig. 6.2, at small $\varepsilon_{\rm m}$ the CNOT gate infidelity is dominated by imperfection of the unitaries $\tilde{U}_0^{\rm t}$ and $\tilde{U}_1^{\rm t}$ (contribution $1 - F_{\tilde{M}U}$), while at large $\varepsilon_{\rm m}$ the leakage contribution $1 - F_{M\tilde{M}}$ dominates (the same result for other detunings Δ). This is because at small $\varepsilon_{\rm m}$ the effect of zz-coupling is important (as discussed in Chapter 5), while at large $\varepsilon_{\rm m}$ the ramps of the pulse become rather short (and high), making the process significantly

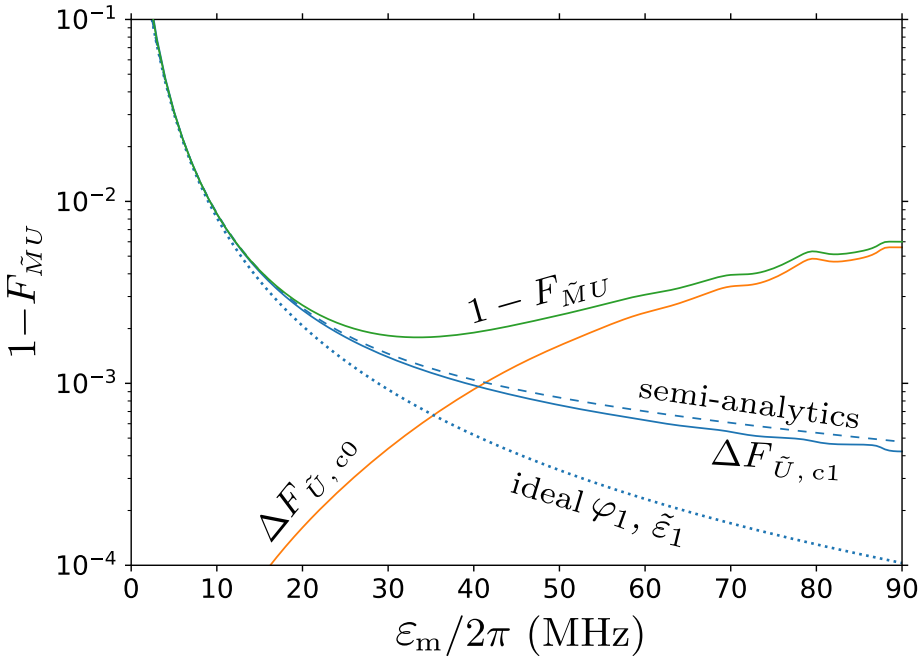

Figure 6.3: Further decomposition of the imperfect-unitary infidelity contribution $1 - F_{\tilde{M}U}$ (green line) into contributions $\Delta F_{\tilde{U},\mathrm{c0}}$ (orange line) and $\Delta F_{\tilde{U},\mathrm{c1}}$ (blue solid line) for the control-qubit states $|0\rangle$ and $|1\rangle$, respectively. The dotted blue line shows analytical approximation for $\Delta F_{\tilde{U},\mathrm{c1}}$ by Eq. (6.4) with ideal values for φ_1 and $\tilde{\varepsilon}_1$, while for the dashed blue line we use semi-analytical values for φ_1 and $\tilde{\varepsilon}_1$ in Eq. (6.4). Parameters are the same as in Fig. 6.2.

non-adiabatic and causing leakages.

6.3 Improper rotation

To clarify the dependence on $\varepsilon_{\rm m}$ of the imperfect-unitary contribution $1 - F_{\tilde{M}U}$ (green line in Fig. 6.2), we draw this line again in Fig. 6.3 (now on semi-logarithmic scale). We also show the numerical results for the contributions $\Delta F_{\tilde{U},\mathrm{c0}}$ and $\Delta F_{\tilde{U},\mathrm{c1}}$ to this line from imperfections of the unitaries $\tilde{U}_0^{\rm t}$ (for the control-qubit state $|0\rangle$) and $\tilde{U}_1^{\rm t}$ (for the control-qubit state $|1\rangle$): orange and blue solid lines in Fig. 6.3, respectively. At small $\varepsilon_{\rm m}$

the main contribution comes from imperfect $\tilde{U}_1^{\rm t}$. This is because we use the drive frequency resonant with the target qubit for the control-qubit state $|0\rangle$ ($\omega_{\rm d} = \omega_{\rm t}^{\rm c0}$), so for the the control-qubit state $|1\rangle$ the drive is off-resonance by ω_{zz} [see Eq. (2.10)]. This detuning produces rotation of the target-qubit state about a tilted axis, instead of the desired x-axis. To check this explanation, we calculate analytically the corresponding infidelity,

$$\Delta F_{\tilde{U},\,\mathrm{c1}} = \frac{2}{5}\,\sin^2(\varphi_1/2)\,\frac{\omega_{zz}^2}{\frac{25}{40}[2\tilde{\varepsilon}_1(\varepsilon_{\rm m})]^2 + \omega_{zz}^2}, \tag{6.4}$$

where the factor 25/40 comes from integration of $\varepsilon^2(t)$ over the pulse shape (4.7) with $\tau_{\rm r}/\tau_{\rm p} = 0.3$ (such integration in only the denominator is an approximation). Dotted blue line in Fig. 6.3 shows this result with φ_1 and $\tilde{\varepsilon}_1$ calculated analytically: $\varphi_1 = (\eta_{\rm c} + \Delta)/2\eta_{\rm c}$ and Eq. (3.5) for $\tilde{\varepsilon}_1$. Dashed blue line shows Eq. (6.4) with φ_1 and $\tilde{\varepsilon}_1$ calculated using the semi-analytical method. We see that both lines fit reasonably well the numerical result (solid blue line) at small $\varepsilon_{\rm m}$, with a better fit using the semi-analytical values for φ_1 and $\tilde{\varepsilon}_1$. Even better fit (almost perfect, not shown) is when the Bloch-sphere evolution due to ω_{zz} and semi-analytical $\tilde{\varepsilon}(\varepsilon(t))$ is integrated over the pulse shape numerically, instead of using Eq. (6.4).

So, the contribution $\Delta F_{\tilde{U},\,\mathrm{c1}}$ to the gate infidelity due to imperfect unitary $\tilde{U}_{\rm t}^{\rm c1}$ is well explained quantitatively. In contrast, we do not have a simple analytical way to find the contribution $\Delta F_{\tilde{U},\,\mathrm{c0}}$ due to imperfect $\tilde{U}_{\rm t}^{\rm c0}$ (orange solid line in Fig. 6.3). Qualitatively, this contribution appears at large $\varepsilon_{\rm m}$ because the interplay between the level repulsions due to g and ε in Fig. 2.3 slightly change the frequency $\omega_{\rm t}^{\rm c0}$, so that there is no longer exact resonance with the drive, and the Bloch-sphere evolution also becomes tilted, thus producing the infidelity. Note that small oscillations of the orange and blue solid lines in

Fig. 6.3 at large $\varepsilon_{\rm m}$ are possibly related to the oscillations of the orange line in Fig. 6.2, which will be discussed later.

6.4 Leakages

The second contribution to the overall gate infidelity $1 - F_{MU}$, which becomes dominating at large $\varepsilon_{\rm m}$ (see Fig. 6.2), is the contribution $1 - F_{M\tilde{M}}$ due to leakage produced by non-adiabaticity during the pulse ramps. From the fidelity definition (4.1), we expect an approximate relation

$$1 - F_{M\tilde{M}} \approx P_{\rm leak}^{\rm out} + \frac{4}{5} P_{\rm leak}^{\rm comp}, \tag{6.5}$$

where $P_{\rm leak}^{\rm out}$ is the probability of leakage outside of the computational subspace, averaged over the initial two-qubit states, and $P_{\rm leak}^{\rm comp}$ is the averaged probability of leakage inside the computational subspace, which for our definition (6.1) means transitions between states $|0\rangle$ and $|1\rangle$ of the control qubit. Note that to average the leakage probability over all initial two-qubit states, it is sufficient to average it over the 4 basis states: $\overline{|0,0\rangle}$, $\overline{|0,1\rangle}$, $\overline{|1,0\rangle}$, and $\overline{|1,1\rangle}$. We have checked the relation (6.5) numerically and it works very well; however, usually either the first or second term in Eq. (6.5) strongly dominates over the other term (depending on the dominating leakage channel).

Figure 6.4 shows again the orange line $1 - F_{M\tilde{M}}$ from Fig. 6.2 (now it is the thick orange line and the scale is semi-logarithmic) and also shows the numerical leakage probabilities (multiplied by the factor 1/4 as in the averaging) for the processes $\overline{|0,0\rangle} \to \overline{|2,0\rangle}$, $\overline{|0,1\rangle} \to \overline{|2,1\rangle}$, $\overline{|0,0\rangle} \to \overline{|2,1\rangle}$, and $\overline{|0,1\rangle} \to \overline{|2,0\rangle}$ (thin solid lines). The sum of the thin solid lines is shown as the dotted brown line. It is very close to the thick orange line [as

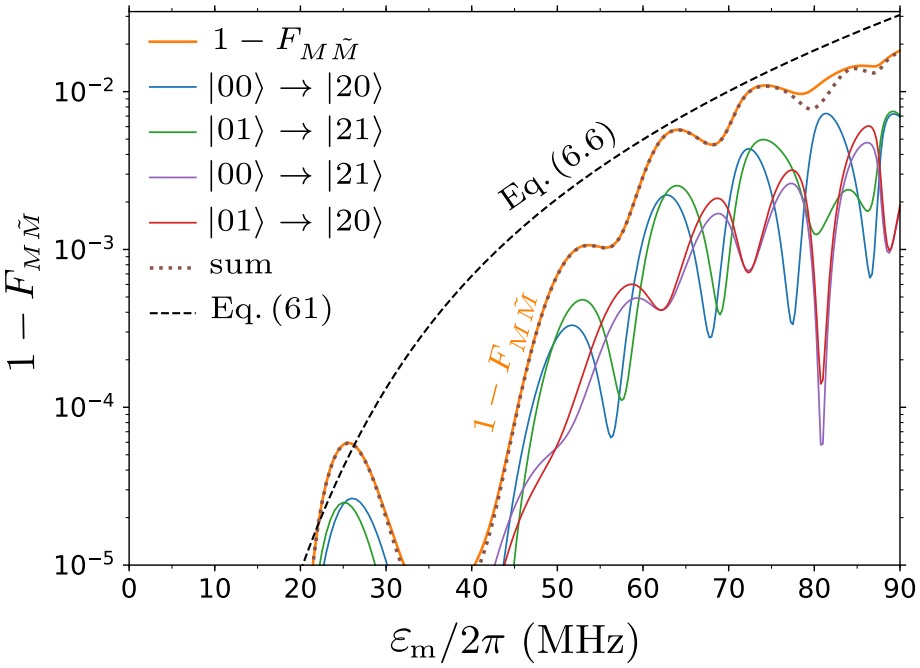

Figure 6.4: Numerical results for the leakage. Thick orange line shows infidelity contribution $1 - F_{M\tilde{M}}$. Four thin solid lines show multiplied by the factor 1/4 probabilities of the main leakage channels: $\overline{|0,0\rangle} \to \overline{|2,0\rangle}$, $\overline{|0,1\rangle} \to \overline{|2,1\rangle}$, $\overline{|0,0\rangle} \to \overline{|2,1\rangle}$, and $\overline{|0,1\rangle} \to \overline{|2,0\rangle}$. The sum of these four lines is shown by the brown dotted line; its closeness to the thick orange line verifies that the infidelity $1 - F_{M\tilde{M}}$ is mainly due to these leakage channels. The black dashed line is the leakage probability estimate given by Eq. (6.6). Parameters are the same as in Fig. 6.2.

expected from Eq. (6.5)], indicating that these are the four dominating leakage channels. A minor difference between the thick orange line and dotted brown line at $\varepsilon_{\rm m}$ close to 80 MHz is due to significance of the additional leakage channels $\overline{|0,1\rangle} \to \overline{|1,2\rangle}$ and $\overline{|0,0\rangle} \to \overline{|1,2\rangle}$ (at this frequency the states $\overline{|2,1\rangle}$ and $\overline{|1,2\rangle}$ become on resonance); similarly, a visible difference at about 40 MHz is because the transitions $|0\rangle \leftrightarrow |1\rangle$ in the control qubit become relatively important.

The main leakage channels in Fig. 6.4 involve the transition $|0\rangle \to |2\rangle$ in the control qubit. This is expected because in the rotating frame $E_0^{(c)} - E_2^{(c)} = \eta - 2\Delta$ is only 40 MHz.

The matrix element of this transition via virtual state $|1\rangle$ is $-\sqrt{2}\,\varepsilon^2/\Delta$. Therefore, the non-adiabatic transition $\overline{|0\rangle_\varepsilon} \to \overline{|2\rangle_\varepsilon}$ during the front ramp with duration $\tau_{\rm r}$ of the pulse (4.7) has the amplitude proportional to the Fourier transform of $d(\varepsilon^2)/dt$ at the frequency $\eta - 2\Delta$. The standard calculations give an estimate of the leakage probability in the control qubit during the front ramp:

$$P_{\overline{|0\rangle_\varepsilon}\to\overline{|2\rangle_\varepsilon}} = \frac{2\pi^4\varepsilon_{\rm m}^4}{\Delta^2(\eta-2\Delta)^6\tau_{\rm r}^4}. \tag{6.6}$$

This probability is shown in Fig. 6.4 by black dashed line. We see that it gives a reasonable (crude) approximation of the infidelity $1 - F_{M\tilde{M}}$ due to leakage (if also multiplied by the factor of 1/4, it goes close to the top of oscillating blue and green solid lines). Such a food fit is somewhat surprising because in deriving Eq. (6.6) we assumed a fixed energy difference $E_0^{(\rm c)} - E_2^{(\rm c)} = \eta - 2\Delta$, while for large ε the difference of eigenenergies, $E_{\overline{|0\rangle_\varepsilon}} - E_{\overline{|2\rangle_\varepsilon}}$, becomes significantly larger, e.g., 60.7 MHz for $\varepsilon/2\pi = 60$ MHz and 84.3 MHz for $\varepsilon/2\pi = 80$ MHz. Therefore, we would expect that Eq. (6.6) should significantly overestimate the actual leakage (note the sixth power of $(\eta - 2\Delta)$ in the denominator). As we checked, Eq. (6.6) still works well because the non-adiabatic transition mainly accumulates during the first half of the ramp, when $\varepsilon(t)$ is not too large.

The oscillations of the solid lines in Fig. 6.4 (leakage probabilities multiplied by 1/4) are easily understandable. The non-adiabatic leakage occurs during both front and rear ramps, and the transition amplitudes are added with a non-zero phase due to the energy difference $E_{\overline{|0\rangle_\varepsilon}} - E_{\overline{|2\rangle_\varepsilon}}$, accumulated between the ramps. So, the oscillations are due to constructive or destructive interference of the leakage contributions from the two ramps. We have checked that the $\varepsilon_{\rm m}$-difference between the peaks in Fig. 6.4 is consistent

with estimates based on numerical increase of $E_{\overline{|0\rangle_\varepsilon}} - E_{\overline{|2\rangle_\varepsilon}}$ with ε. The oscillations in the probabilities of individual leakage channels lead to the oscillations of their sum, thus explaining oscillations of $1 - F_{M\tilde{M}}$ in Fig. 6.2 and oscillations of the overall CNOT gate infidelity $1 - F_{MU}$ in Fig. 6.1 at large $\varepsilon_{\rm m}$.

Note that in Fig. 6.4 the leakage channels $\overline{|0,0\rangle} \to \overline{|2,0\rangle}$ and $\overline{|0,1\rangle} \to \overline{|2,1\rangle}$ (with non-changing state of the target qubit) have higher probabilities than for the leakage channels with changing state of the target qubit. This is because $|\varphi_0| \ll \pi$ in the interesting range of $\varepsilon_{\rm m}$ – see Fig. 5.3, so the target-qubit state does not change much during the pulse when the control-qubit state is $|0\rangle$. In the opposite limit, $|\pi - \varphi_0| \ll \pi$, we would expect all four leakage channels to have approximately the same strength, and also would not expect significant oscillations (because the two ramps would mainly contribute to different channels).

Besides the detailed analysis of leakage contribution $1 - F_{M\tilde{M}}$ for the detuning $\Delta/2\pi = 130$ MHz, we have also analyzed the leakage for other values of the detuning in Fig. 6.1. The case of $\Delta/2\pi = 190$ MHz is similar (the same dominating leakage channels) and Eq. (6.6) still works well; however, $|\eta - 2\Delta|$ is larger (80 MHz instead of 40 MHz), so the leakage becomes significant only at larger values of $\varepsilon_{\rm m}$. Also, a very large value of the green line in Fig. 6.1 at $\varepsilon_{\rm m}/2\pi \simeq 70$ MHz is due to an additional leakage channel $\overline{|0,1\rangle} \to \overline{|1,2\rangle}$, which is due to a resonance between these states. For the detuning $\Delta/2\pi$ of 70 MHz and -70 MHz (brown and red lines in Fig. 6.1), the main leakage is between states $\overline{|0\rangle_\varepsilon}$ and $\overline{|1\rangle_\varepsilon}$ of the control qubit due to non-adiabaticity during the ramps.

Thus, in this chapter we have shown that in our model the error budget of the CR gate consists of two main contributions: imperfection of the unitary operation at small drive amplitudes and the leakage at large drive amplitudes. At the optimal drive amplitude, the infidelity is on the order of 10^{-3}. However, we did not take into account contributions from decoherence and also from possible problems caused by a strong drive of the control qubit (e.g., due to a resonance between a two-level system and $E_{\overline{|0\rangle_\varepsilon}} - E_{\overline{|n\rangle_\varepsilon}}$ or $E_{\overline{|1\rangle_\varepsilon}} - E_{\overline{|n\rangle_\varepsilon}}$). Note that a strong leakage makes the CR gate operation impractical for the detuning Δ close to 0, $\eta_c/2$, η_c, $3\eta_c/2$, etc.

Chapter 7

Dependence on parameters

A convenient way to present numerical results [53] is to paratetrically plot infidelity $1 - F_{MU}$ versus CNOT gate duration $\tau_{\rm p}^{\rm CNOT}$, with both quantities being functions of the drive amplitude $\varepsilon_{\rm m}$. Figure 7.1 presents such a plot for the results shown in Figs. 5.1 and 6.1 for the detuning values $\Delta/2\pi = -70$, 70, 130, and 190 MHz, while other parameters are $g/2\pi = 3$ MHz, $\eta_{\rm c}/2\pi = \eta_{\rm t}/2\pi = 300$ MHz, $\omega_{\rm d} = \omega_{\rm t}^{\rm c0}$, and $\tau_{\rm r}/\tau_{\rm p} = 0.3$. Increase of $\varepsilon_{\rm m}$ corresponds to moving from right to left along the lines. The main observation is that for each Δ the line is very steep at the left, which naturally corresponds to a limit on decreasing the duration of the CNOT gate. Among the plotted lines, the line for the detuning of 190 MHz gives the shortest duration (consistent with our discussion in Sec. 3.3); however, it does not give the best fidelity.

In Fig. 7.2 we show the results for slightly different drive frequencies for the qubit detunings of 70 MHz (brown lines) and 190 MHz (green lines). Besides using the drive frequency resonant with the target qubit when the control-qubit state is $|0\rangle$ (solid lines,

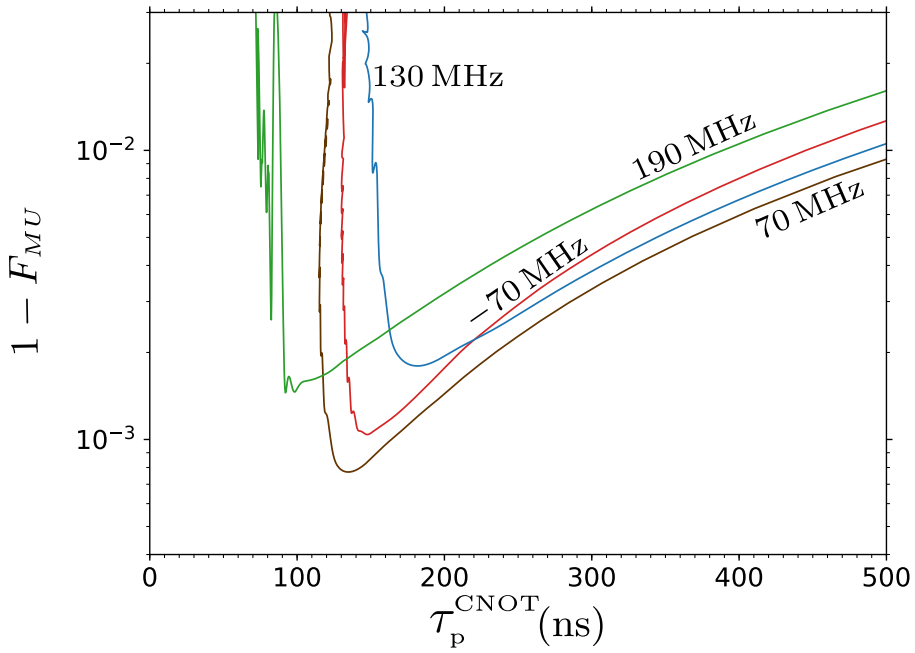

Figure 7.1: Parametric plot for the CNOT gate infidelity $1 - F_{MU}$ versus the CNOT gate duration $\tau_{\rm p}^{\rm CNOT}$ (the running parameter is $\varepsilon_{\rm m}$) for the detunings $\Delta/2\pi = -70$, 70, 130, and 190 MHz. We assume $g/2\pi = 3$ MHz, $\eta_{\rm c}/2\pi = \eta_{\rm t}/2\pi = 300$ MHz, $\omega_{\rm d} = \omega_{\rm t}^{\rm c0}$, and $\tau_{\rm r}/\tau_{\rm p} = 0.3$.

$\omega_{\rm d} = \omega_{\rm t}^{\rm c0}$, $\delta = \omega_{\rm t} - \omega_{\rm t}^{\rm c0}$), we also use the drive resonant with the target qubit when the control-qubit state is $|1\rangle$ (dotted lines, $\omega_{\rm d} = \omega_{\rm t}^{\rm c1}$), and also show the case of the drive frequency exactly in between (dashed lines, $\omega_{\rm d} = (\omega_{\rm t}^{\rm c0} + \omega_{\rm t}^{\rm c1})/2$). Note that $\omega_{\rm t}^{\rm c1} - \omega_{\rm t}^{\rm c0} = \omega_{zz}$ is 127 kHz and 200 kHz for the detunings of 70 MHz and 190 MHz, respectively [see Eq. (2.11)]. We see that this small change of the drive frequency practically does not affect the natural limit for $\tau_{\rm p}^{\rm CNOT}$; however, it may very significantly affect the infidelity. For example, for $\Delta/2\pi = 70$ MHz the minimum infidelity is 1.7×10^{-4} for $\omega_{\rm d} = (\omega_{\rm t}^{\rm c0} + \omega_{\rm t}^{\rm c1})/2$, while it is 7.7×10^{-4} for $\omega_{\rm d} = \omega_{\rm t}^{\rm c0}$. We have checked that this small change of the drive frequency practically does not affect the leakage $1 - F_{M\tilde{M}}$, but affects significantly the infidelity contribution $1 - F_{\tilde{M}U}$ due to imperfection of the unitary operation. This is exactly what is

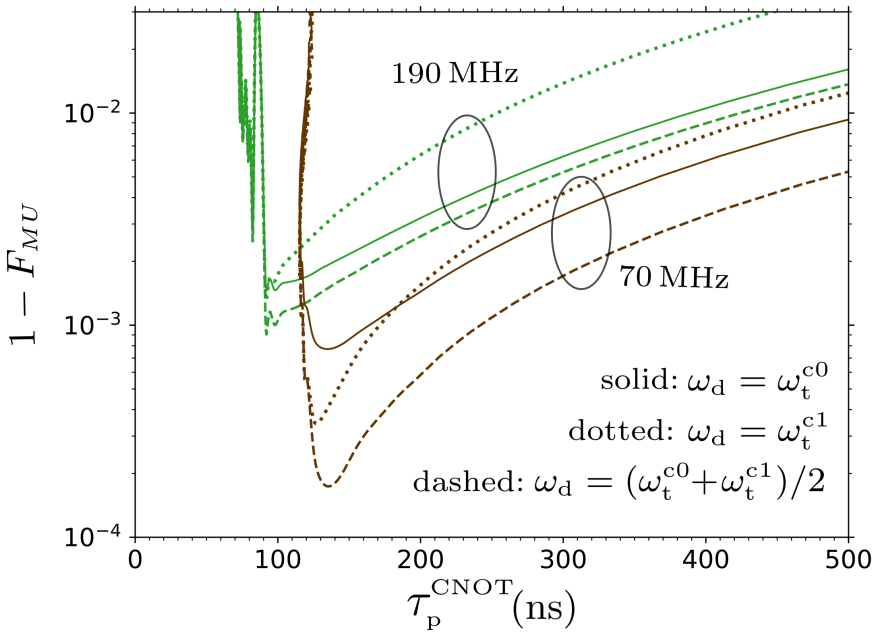

Figure 7.2: CNOT gate infidelity $1 - F_{MU}$ versus duration τ_p^{CNOT} (both are functions of ε_m) for $\Delta/2\pi = 70$ and 190 MHz and the drive frequency on resonance with the target qubit for the control qubit either in the state $|0\rangle$ (solid lines, $\omega_d = \omega_t^{c0}$) or in the state $|1\rangle$ (dotted lines, $\omega_d = \omega_t^{c1}$) or exactly in between (dashed lines, $\omega_d = (\omega_t^{c0} + \omega_t^{c1})/2$). Other parameters are as in Fig. 7.1.

expected from the analysis in Chapter. 6, since the unitary imperfection is due to imperfect resonance between the drive and the target qubit. As we see from the numerical results, the drive frequency $\omega_d = (\omega_t^{c0} + \omega_t^{c1})/2$ typically gives a better optimized fidelity than for $\omega_d = \omega_t^{c0}$ or $\omega_d = \omega_t^{c1}$.

In all previous numerical plots we assumed the qubit-qubit coupling $g/2\pi = 3$ MHz. Figure 7.3 shows the CNOT gate infidelity for $g/2\pi = 1.5$, 3, and 6 MHz, while $\Delta/2\pi = 190$ MHz and other parameters are as in Fig. 7.1. As expected, for minima of the lines in Fig. 7.3, the CNOT gate duration decreases with increasing g as g^{-1}; however, we see that the infidelity increases crudely as g^2. Increase of g also increases undesired

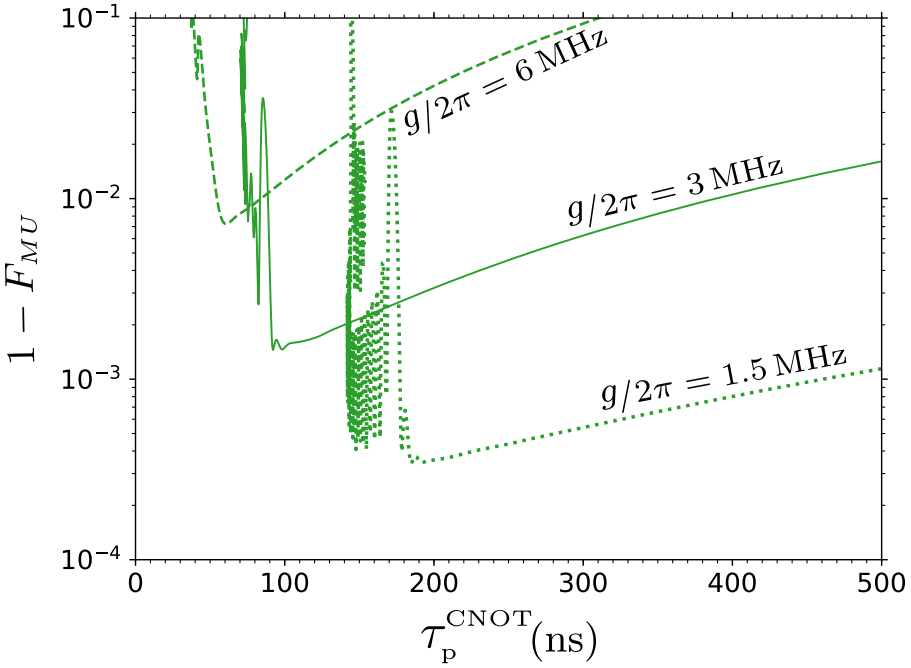

Figure 7.3: CNOT gate infidelity $1 - F_{MU}$ versus duration $\tau_{\rm p}^{\rm CNOT}$ for $\Delta/2\pi = 190$ MHz and several values of the qubit-qubit coupling: $g/2\pi$=1.5, 3, and 6 MHz. Other parameters are as in Fig. 7.1.

zz-interaction of idling qubits [62] and therefore cannot be used as a simple way to reduce the CNOT gate duration in an experiment.

In Fig. 7.4 we numerically analyze dependence on the relative duration of the pulse ramp by changing the ratio $\tau_{\rm r}/\tau_{\rm p}$ in the pulse shape (4.7): $\tau_{\rm r}/\tau_{\rm p} = 0.1$, 0.2, 0.3, 0.4, and 0.5 (other parameters are as in Fig. 7.1 with $\Delta/2\pi = 190$ MHz.) For clarity we do not show all oscillations on the left, cutting the lines at some maxima of the oscillations. We see that at the right side of the graph (long $\tau_{\rm p}^{\rm CNOT}$) it is better to have the longest possible ramp, $\tau_{\rm r}/\tau_{\rm p} = 0.5$. However, in the optimal range of short $\tau_{\rm p}^{\rm CNOT}$ with still small infidelity, the line with $\tau_{\rm r}/\tau_{\rm p} = 0.3$ shows the best performance, which can be understood as the following trade-off. For longer ramps and the same $\tau_{\rm p}^{\rm CNOT}$, we need to use larger $\varepsilon_{\rm m}$ that increases the

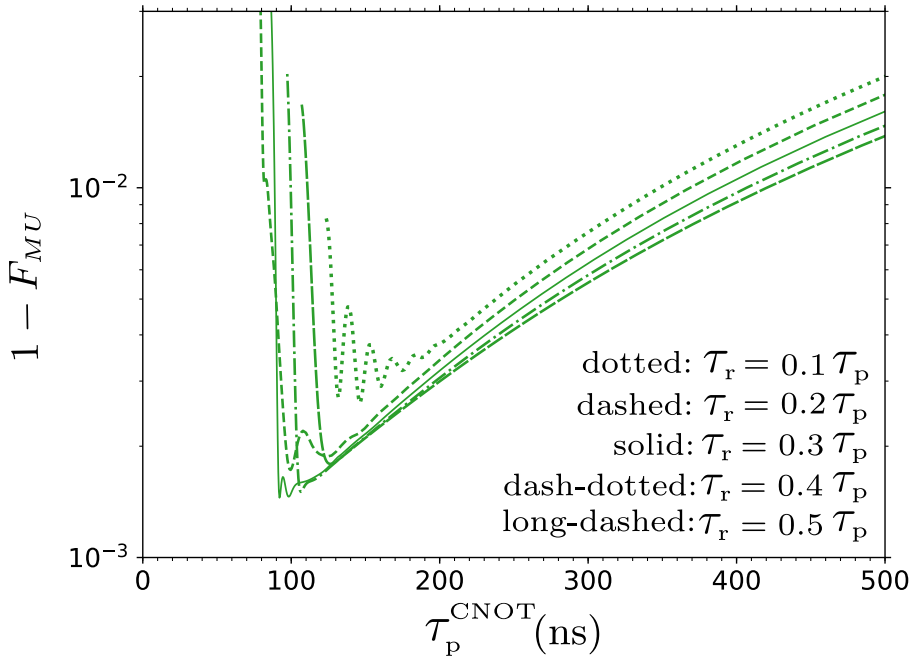

Figure 7.4: CNOT gate infidelity $1 - F_{MU}$ versus duration $\tau_{\rm p}^{\rm CNOT}$ for $\Delta/2\pi = 190$ MHz and several values of the relative duration of the pulse ramps: $\tau_{\rm r}/\tau_{\rm p} = 0.1$ (dotted line), 0.2 (dashed line), 0.3 (solid line), 0.4 (dash-dotted line), and 0.5 (long-dashed line). Other parameters are as in Fig. 7.1. The lines are cut at the left for clarity.

leakage (even though the ramp is smoother), while for shorter ramps and the same $\tau_{\rm p}^{\rm CNOT}$, the leakage is also increased because the ramp is too short and consequently non-adiabatic (even though $\varepsilon_{\rm m}$ is smaller). Thus, the ramps should be sufficiently smooth, but it is still beneficial to have a flat part of the pulse.

Finally, let us discuss the effect of the microwave crosstalk, which is always present in experiments [38, 40, 43]. To include it, we need to add the crosstalk Hamiltonian

$$H_{\rm ct} = \sum\nolimits_m c_{\rm ct}\,\varepsilon(t)\sqrt{m}\,|n,m\rangle\langle n,m-1| + \text{h.c.}, \tag{7.1}$$

which describes the microwave field applied directly to the target qubit. The crosstalk coefficient $c_{\rm ct}$ can in general be complex (and experimental results seem to indicate it

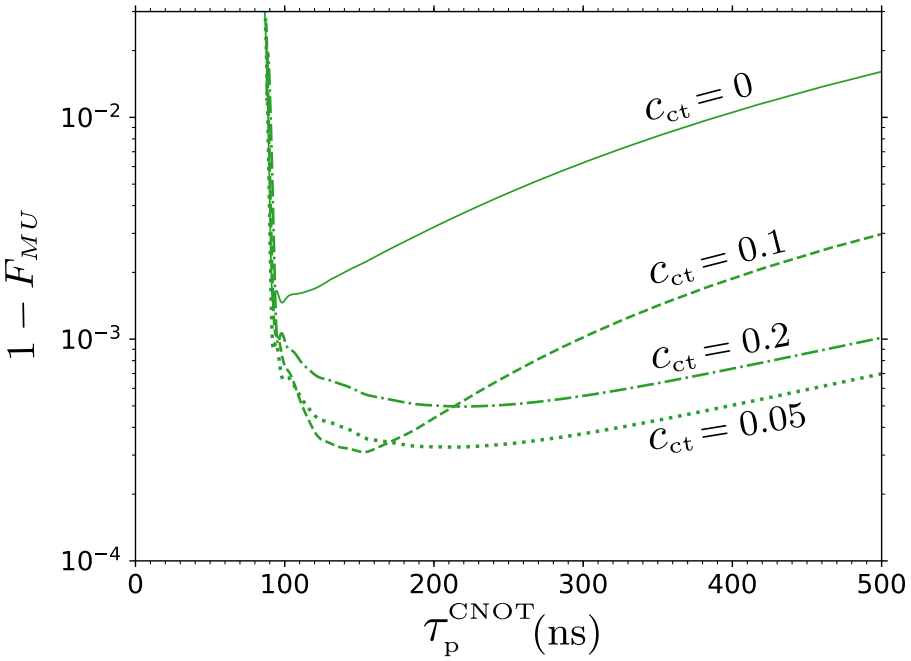

Figure 7.5: CNOT gate infidelity $1 - F_{MU}$ versus duration $\tau_{\rm p}^{\rm CNOT}$ for $\Delta/2\pi = 190$ MHz and several values of the microwave crosstalk coefficient: $c_{\rm ct} = 0$ (solid line), 0.05 (dotted line), 0.1 (dashed line) and 0.2 (dash-dotted line). Other parameters are as in Fig. 7.1. The lines are cut at the left for clarity.

[38, 51]); however, it is not clear what could be an experimental reason for a significant phase shift. For simplicity we will assume a real $c_{\rm ct}$ below. In the ideal and semi-analytical theory, the crosstalk with real $c_{\rm ct}$ does not affect the results, except adding the phase $\varphi_{\rm ct} = \int_0^{\tau_{\rm p}} 2c_{\rm ct}\,\varepsilon(t)\,dt$ to both φ_0 and φ_1. However, it affects the numerical results because the crosstalk changes the Bloch-sphere angle of tilt caused by the effect of ω_{zz}.

Figure 7.5 shows numerical results for several values of the crosstalk coefficient $c_{\rm ct}$ (the parameters are as in Fig. 7.1 with $\Delta/2\pi = 190$ MHz). We see that the crosstalk improves fidelity. This improvement can be easily understood. The crosstalk does not affect leakage, but it decreases the imperfect-unitary contribution $1 - F_{M\tilde{M}}$ because now

the drive detuning $\omega_{\rm d} - \omega_{\rm t}^{\rm c1}$ should be compared with a larger Rabi frequency $\tilde{\varepsilon}_1 + c_{\rm ct}\varepsilon$ instead of $\tilde{\varepsilon}_1$, and therefore the resulting tilt of the Bloch-sphere evolution is smaller (the same effect for the control-qubit state $|0\rangle$ if the signs of $\tilde{\varepsilon}_0$ and $c_{\rm ct}\varepsilon$ coincide). Thus, somewhat unexpectedly, the microwave crosstalk can improve the gate fidelity. However, this improvement is significant only if the effect of ω_{zz} is significant. For example, if in an experiment the infidelity is mainly determined by leakage and decoherence, then the crosstalk will not improve fidelity.

Chapter 8

Conclusion

In this thesis we have analyzed analytically, semi-analytically, and numerically the operation of the Cross-Resonance gate for superconducting qubits, focusing on using the CR gate to realize the CNOT operation [38, 40, 45]. Our model has been based on the Hamiltonian (2.1)–(2.8) and simple pulse shape (no echo sequence).

The analytical theory gives Eq. (3.7) for the effective drive amplitude $\tilde{\varepsilon}_n$ of the target qubit, which depends on the control-qubit state $|n\rangle$. However, the analytics can be used only for sufficiently small (and not too small) physical drive amplitude ε. The next-order analytics (see 3.2) slightly widens the applicability range; however, it is still inapplicable in the practically interesting range of ε.

We have found that the speed of the CR gate and the compensating single-qubit rotations can be obtained very accurately by a sufficiently simple semi-analytical theory, discussed in 3.3. This theory is based on solving the one-qubit time-independent Schrödinger equation (3.15). The semi-analytical theory depends on only two parameters: dimension-

less qubit-qubit detuning Δ/η_c (normalization is the control-qubit anharmonicity η_c) and dimensionless drive amplitude ε/η_c. The dimensionless speed of the CR gate as a function of these two parameters is shown in Fig. 3.4. The CR gate speed cannot be increased indefinitely by increasing the drive amplitude ε; the maximum speed (as a function of Δ/η_c) and the corresponding drive amplitude are shown in Fig. 3.5. As follows from Figs. 3.4 and 3.5, the best operation of the CR gate is expected for the detuning within the range $0.5\,\eta_c < \Delta < \eta_c$.

Full numerical approach (discussed in Chapter 4) is mainly needed to calculate intrinsic fidelity of the CNOT-equivalent CR gate. The numerical results depend on the pulse shape, for which we use the simple cosine-ramp model, Eq. (4.7). Most importantly, the infidelity $1-F_{MU}$ has a minimum as a function of the mid-pulse drive amplitude ε_m. The minimum value depends on the detuning Δ (Figs. 6.1 and 7.1), and for typical parameters used in this thesis the optimal infidelity is on the order of 10^{-3} (though it approaches 10^{-4} for some parameters, and in principle the theoretical infidelity can be arbitrarily small for complicated pulse shapes [53]).

Our model does not include decoherence, so the error budget of the gate consists of two contributions: due to imperfect unitary operations and due to leakages [Eq. (6.2)]. The imperfect unitary dominates at small ε_m. The mechanism of this imperfection is related to the zz-interaction of the qubits [Eq. (2.10)], which makes the target-qubit frequency dependent on the control-qubit state ($\omega_t^{c1} - \omega_t^{c0} = \omega_{zz}$), and therefore makes it impossible to use a drive frequency exactly on resonance with the target qubit in both cases (for the control-qubit states $|0\rangle$ and $|1\rangle$). Because of this contribution into the error budget, at small

$\varepsilon_{\rm m}$ the gate infidelity is very sensitive to small changes in the drive frequency (Fig. 7.2), and the microwave crosstalk can improve fidelity (Fig. 7.5).

The other contribution into the error budget, which dominates at large drive amplitudes $\varepsilon_{\rm m}$, is due to leakages. The main leakage is in the strongly-driven control qubit and is caused by non-adiabaticity during the ramps of the pulse. Depending on the ratio $\Delta/\eta_{\rm c}$ between the detuning and control-qubit anharmonicity, the main leakage mechanism can be either $|0\rangle \leftrightarrow |1\rangle$ (between the control-qubit states $|0\rangle$ and $|1\rangle$) or $|0\rangle \rightarrow |2\rangle$ or some other leakage channel. In particular, for $|\Delta| \ll \eta_{\rm c}$ there is a strong leakage $|0\rangle \leftrightarrow |1\rangle$ because the drive frequency is near resonance with the control qubit. Similarly, for $|\Delta - \eta_{\rm c}/2| \ll \eta_{\rm c}$ there is a strong leakage $|0\rangle \rightarrow |2\rangle$ because in this case the energy difference between states $|2\rangle$ and $|0\rangle$ of the control qubit is near resonance with doubled frequency of the drive. In some cases we also observed a significant leakage for the channel $\overline{|0,1\rangle} \rightarrow \overline{|1,2\rangle}$ (when it becomes near-resonant).

Strong leakage makes the CR gate operation impractical when detuning Δ is close to 0, $\eta_{\rm c}/2$, $\eta_{\rm c}$, $3\eta_{\rm c}/2$, etc. Therefore, we would expect the best operation of the CR gate for the detuning within the range $0.6\,\eta_{\rm c} < \Delta < 0.8\,\eta_{\rm c}$ (see Figs. 3.4 and 3.5). Another reasonable range (which requires smaller drive amplitudes) is $0.2\,\eta_{\rm c} < \Delta < 0.3\,\eta_{\rm c}$.

Crudely, the CNOT-equivalent gate duration $\tau_{\rm p}^{\rm CNOT}$ (optimized over $\varepsilon_{\rm m}$) is comparable to π/g, with a coefficient somewhat larger or smaller than 1, depending on $\Delta/\eta_{\rm c}$ – see Fig. 7.1. The optimized intrinsic infidelity for a simple pulse shape (4.7) is crudely comparable to $(g/\eta_{\rm c})^2$ (as follows from scaling of ω_{zz} and $\tau_{\rm p}^{\rm CNOT}$), with a coefficient typically about 10^0–$10^{1.5}$, depending on drive frequency, $\Delta/\eta_{\rm c}$, crosstalk, etc. We have found that to

reduce non-adiabatic leakage, the ramps of the pulse should occupy a significant fraction of the pulse duration; however, the flat part in the middle of the pulse should not be shortened to zero.

A crude estimate of the CR gate infidelity contribution due to decoherence (within the computational subspace only) is given by Eq. (4.10). However, for large drive amplitudes the bare state $|2\rangle$ and higher states of the control qubit are significantly occupied; their decoherence is typically much faster than in the computational subspace and therefore can significantly increase the gate infidelity. Another potential mechanism for experimental CR gate infidelity is due to two-level systems (TLSs) produced by impurities. A strong drive changes the effective energy levels in the control qubit by about one hundred MHz, and therefore the TLSs can become on resonance with the control qubit during the ramp of the pulse. Moreover, large drive amplitude makes multi-photon processes easily possible, and therefore TLSs can become resonant with combinational frequencies for many channels (similar to the situation for fast measurement of a qubit).

Note that in this thesis we did not explicitly take into account the resonator, providing coupling between the qubits; instead we replaced it with an equivalent direct coupling. It would be interesting to repeat our numerical simulations, taking into account the resonator levels explicitly. However, we do not expect a significant modification of the results because the additional non-adiabatic effects should be suppressed by typically large detuning between the resonator and qubits. It would also be interesting to include decoherence into the simulations; however, it is not obvious what is a proper model for decoherence of higher levels, relevant to actual experimental situations.

We hope that some experimental group will carry out detailed measurements of the CNOT duration and error budget of the CR gate as functions of the drive amplitude, drive frequency, detuning, and pulse shape. It will be interesting (and important for the CR gate application in quantum computing) to compare experimental results with our theoretical findings.

Bibliography

[1] R. P. Feynman, Simulating physics with computers, Int. J. Theor. Phys. **21**, 467 (1982).

[2] C. H. Bennett and G. Brassard, Quantum cryptography: Public key distribution and coin tossing, in *Proceedings of IEEE International Conference on Computers, Systems and Signal Processing*, Vol. 175 (1984) p. 175.

[3] D. Deutsch, Quantum theory, the Church-Turing principle and the universal quantum computer, Proc. R. Soc. Lond. A **400**, 97 (1985).

[4] P. W. Shor, Algorithms for quantum computation: discrete logarithms and factor- ing, in *Proceedings 35th Annual Symposium on Foundations of Computer Science* (1994) p. 124.

[5] P. Shor, Polynomial-Time Algorithms for Prime Factorization and Discrete Logarithms on a Quantum Computer, SIAM J. Comput. **26**, 1484 (1997), arXiv:quant-ph/9508027.

[6] L. K. Grover, A fast quantum mechanical algorithm for database search, in *Annual ACM symposium on theory of computing* (ACM, 1996) p. 212.

[7] P. W. Shor, Scheme for reducing decoherence in quantum computer memory, Phys. Rev. A **52**, 2493(R) (1995).

[8] A. Steane, Multiple-particle interference and quantum error correction, Proc. R. Soc. Lond. A **452**, 2551 (1996).

[9] A. R. Calderbank and P. W. Shor, Good quantum error-correcting codes exist, Phys. Rev. A **54**, 1098 (1996).

[10] A. Y. Kitaev, Fault-tolerant quantum computation by anyons, Ann. Phys. **303**, 2 (2003).

[11] M. W. Johnson, M. H. S. Amin, S. Gildert, T. Lanting, F. Hamze, N. Dickson, R. Harris, A. J. Berkley, J. Johansson, P. Bunyk, E. M. Chapple, C. Enderud, J. P. Hilton, K. Karimi, E. Ladizinsky, N. Ladizinsky, T. Oh, I. Perminov, C. Rich, M. C. Thom, E. Tolkacheva, C. J. S. Truncik, S. Uchaikin, J. Wang, B. Wilson, and G. Rose, Quantum annealing with manufactured spins, Nature **473**, 194 (2011).

[12] T. Albash and D. A. Lidar, Adiabatic quantum computation, Rev. Mod. Phys. **90**, 015002 (2018).

[13] D. P. DiVincenzo, The Physical Implementation of Quantum Computation, Fortschr. Phys. **48**, 771 (2000).

[14] K. K. Likharev, *Dynamics of Josephson Junctions and Circuits* (CRC Press, New York, 1986).

[15] Y. Nakamura, Yu. A. Pashkin, and J. S. Tsai, Nature **398**, 786 (1999).

[16] J. E. Mooij, T. P. Orlando, L. Levitov, L. Tian, C. H. v. d. Wal, and S. Lloyd, Josephson Persistent-Current Qubit, Science **285**, 1036 (1999).

[17] I. Chiorescu, Y. Nakamura, C. J. P. M. Harmans, and J. E. Mooij, Coherent Quantum Dynamics of a Superconducting Flux Qubit, Science **299**, 1869 (2003).

[18] J. M. Martinis, S. Nam, J. Aumentado, and C. Urbina, Rabi Oscillations in a Large Josephson-Junction Qubit, Phys. Rev. Lett. **89**, 117901 (2002).

[19] M. Steffen, M. Ansmann, R. McDermott, N. Katz, R. C. Bialczak, E. Lucero, M. Neeley, E. M. Weig, A. N. Cleland, and J. M. Martinis, State Tomography of Capacitively Shunted Phase Qubits with High Fidelity, Phys. Rev. Lett. **97**, 050502 (2006).

[20] D. C. McKay, C. J. Wood, S. Sheldon, J. M. Chow, and J. M. Gambetta, Efficient Z gates for quantum computing, Phys. Rev. A **96**, 022330 (2017).

[21] J. Kelly, R. Barends, A. G. Fowler, A. Megrant, E. Jeffrey, T. C. White, D. Sank, J. Y. Mutus, B. Campbell, Y. Chen, Z. Chen, B. Chiaro, A. Dunsworth, I. C. Hoi, C. Neill, P. J. J. OMalley, C. Quintana, P. Roushan, A. Vainsencher, J. Wenner, A. N. Cleland, and J. M. Martinis, State preservation by repetitive error detection in a superconducting quantum circuit, Nature **519**, 66 (2015).

[22] M. Rol, C. Bultink, T. OBrien, S. de Jong, L. Theis, X. Fu, F. Luthi, R. Vermeulen, J. de Sterke, A. Bruno, D. Deurloo, R. Schouten, F. Wilhelm, and L. DiCarlo, Restless Tuneup of High-Fidelity Qubit Gates, Phys. Rev. Appl. **7**, 041001 (2017).

[23] C. Neill, P. Roushan, K. Kechedzhi, S. Boixo, S. V. Isakov, V. Smelyanskiy, A. Megrant, B. Chiaro, A. Dunsworth, K. Arya, R. Barends, B. Burkett, Y. Chen, Z. Chen, A. Fowler, B. Foxen, M. Giustina, R. Graff, E. Jeffrey, T. Huang, J. Kelly, P. Klimov, E. Lucero, J. Mutus, M. Neeley, C. Quintana, D. Sank, A. Vainsencher, J. Wenner, T. C. White, H. Neven, and J. M. Martinis, Science **360**, 195 (2018).

[24] A. Kandala, A. Mezzacapo, K. Temme, M. Takita, M. Brink, J. M. Chow, and J. M. Gambetta, Nature **549**, 242 (2017).

[25] K. S. Chou, J. Z. Blumoff, C. S. Wang, P. C. Reinhold, C. J. Axline, Y. Y. Gao, L. Frunzio, M. H. Devoret, L. Jiang, and R. J. Schoelkopf, Nature **561**, 7723 (2018).

[26] S. S. Hong, A. T. Papageorge, P. Sivarajah, G. Crossman, N. Dider, A. M. Polloreno, E. A. Sete, S. W. Turkowski, M. P. da Silva, and B. R. Johnson, arXiv:1901.08035.

[27] S. Hacohen-Gourgy, L. S. Martin, E. Flurin, V. V. Ramasesh, K. B. Whaley, and I. Siddiqi, Nature **538**, 491 (2016).

[28] K. J. Satzinger, Y. P. Zhong, H.-S. Chang, G. A. Peairs, A. Bienfait, M.-H. Chou, A. Y. Cleland, C. R. Conner, E. Dumur, J. Grebel, I. Gutierrez, B. H. November, R. G. Povey, S. J. Whiteley, D. D. Awschalom, D. I. Schuster, and A. N. Cleland, Nature **563**, 661 (2018).

[29] A. D. King, J. Carrasquilla, I. Ozfidan, J. Raymond, E. Andriyash, A. Berkley, M. Reis, T. M. Lanting, R. Harris, G. Poulin-Lamarre, A. Y. Smirnov, C. Rich, F. Altomare, P. Bunyk, J. Whittaker, L. Swenson, E. Hoskinson, Y. Sato, M. Volkmann, E. Ladizinsky, M. Johnson, J. Hilton, and M. H. Amin, Nature **560**, 456 (2018).

[30] P. Kurpiers, P. Magnard, T. Walter, B. Royer, M. Pechal, J. Heinsoo, Y. Salathe, A. Akin, S. Storz, J. C. Besse, S. Gasparinetti, A. Blais, and A. Wallraff, Nature **558**, 264 (2018).

[31] Z. K. Minev, S. O. Mundhada, S. Shankar, P. Reinhold, R. Gutierrez-Jauregui, R. J. Schoelkopf, M. Mirrahimi, H. J. Carmichael, and M. H. Devoret, arXiv:1803.00545.

[32] Y. Masuyama, K. Funo, Y. Murashita, A. Noguchi, S. Kono, Y. Tabuchi, R. Yamazaki, M. Ueda, and Y. Nakamura, Nat. Comm. **9**, 1291 (2018).

[33] J. Koch, T. M. Yu, J. Gambetta, A. A. Houck, D. I. Schuster, J. Majer, A. Blais, M. H. Devoret, S. M. Girvin, and R. J. Schoelkopf, Phys. Rev. A **76**, 042319 (2007).

[34] R. Barends, J. Kelly, A. Megrant, D. Sank, E. Jeffrey, Y. Chen, Y. Yin, B. Chiaro, J. Mutus, C. Neill, P. O'Malley, P. Roushan, J. Wenner, T. C. White, A. N. Cleland, and J. M. Martinis, Phys. Rev. Lett. **111**, 080502 (2013).

[35] Y. Chen, C. Neill, P. Roushan, N. Leung, M. Fang, R. Barends, J. Kelly, B. Campbell, Z. Chen, B. Chiaro, A. Dunsworth, E. Jeffrey, A. Megrant, J. Y. Mutus, P. J. J. O'Malley, C. M. Quintana, D. Sank, A. Vainsencher, J. Wenner, T. C. White, M. R. Geller, A. N. Cleland, and J. M. Martinis, Phys. Rev. Lett. **113**, 220502 (2014).

[36] M. A. Nielsen and I. L. Chuang, *Quantum Computation and Quantum Information* (Cambridge University Press, Cambridge, 2000).

[37] R. Barends, J. Kelly, A. Megrant, A. Veitia, D. Sank, E. Jeffrey, T.C. White, J. Mutus, A.G. Fowler, B. Campbell, Y. Chen, Z. Chen, B. Chiaro, A. Dunsworth, C. Neill, P. O'Malley, P. Roushan, A. Vainsencher, J. Wenner, A. N. Korotkov, A. N. Cleland, and J. M. Martinis, Nature **508**, 500 (2014).

[38] S. Sheldon, E. Magesan, J. M. Chow, and J. M. Gambetta, Phys. Rev. A **93**, 060302 (2016).

[39] C. Rigetti and M. Devoret, Phys. Rev. B **81**, 134507 (2010).

[40] J. M. Chow, A. D. Córcoles, J. M. Gambetta, C. Rigetti, B. R. Johnson, J. A. Smolin, J. R. Rozen, G. A. Keefe, M. B. Rothwell, M. B. Ketchen, and M. Steffen, Phys. Rev. Lett. **107**, 080502 (2011).

[41] G. S. Paraoanu, Phys. Rev. B **74**, 140504 (2006).

[42] P. C. de Groot, J. Lisenfeld, R. N. Schouten, S. Ashhab, A. Lupaşcu, C. J. P. M. Harmans, and J. E. Mooij, Nat. Phys. **6**, 763 (2010).

[43] J. M. Chow, J. M. Gambetta, A. D. Córcoles, S. T. Merkel, J. A. Smolin, C. Rigetti, S. Poletto, G. A. Keefe, M. B. Rothwell, J. R. Rozen, M. B. Ketchen, and M. Steffen, Phys. Rev. Lett. **109**, 060501 (2012).

[44] A. D. Córcoles, J. M. Gambetta, J. M. Chow, J. A. Smolin, M. Ware, J. Strand, B. L. T. Plourde, and M. Steffen, Phys. Rev. A **87**, 030301 (2013).

[45] A. Córcoles, E. Magesan, S. J. Srinivasan, A. W. Cross, M. Steffen, J. M. Gambetta, and J. M. Chow, Nat. Commun. **6**, 6979 (2015).

[46] M. Takita, A. D. Córcoles, E. Magesan, B. Abdo, M. Brink, A. Cross, J. M. Chow, and J. M. Gambetta, Phys. Rev. Lett. **117**, 210505 (2016).

[47] M. Ware, Ph.D. thesis, Syracuse University (2015), Chapter 4.

[48] R. Naik, B. Mitchell, U. Baek, D. Dahlen, J. M. Kreikebaum, V. Ramasesh, M. Blok, and I. Siddiqi, APS March Meeting 2019, Abstract L29.6.

[49] P. C. de Groot, S. Ashhab, A. Lupaşcu, L. DiCarlo, F. Nori, C. J. P. M. Harmans and J. E. Mooij, New J. Phys. **14**, 073038 (2012).

[50] J. M. Gambetta, in *Quantum Information Processing: Lecture Notes of the 44th IFF Spring School*, edited by D. P. DiVincenzo (Forschungszentrum Jülich, Jülich, 2013), Chapter B4.

[51] E. Magesan and J. M. Gambetta, arXiv:1804.04073 (2018).

[52] D. Willsch, M. Nocon, F. Jin, H. De Raedt, and K. Michielsen, Phys. Rev. A **96**, 062302 (2017).

[53] S. Kirchhoff, T. Keßler, P. J. Liebermann, E. Assémat, S. Machnes, F. Motzoi, and F. K. Wilhelm, Phys. Rev. A **97**, 042348 (2018).

[54] S. E. Economou and E. Barnes, Phys. Rev. B **91**, 161405(R) (2015).

[55] J. L. Allen, R. Kosut, J. Joo, P. Leek, and E. Ginossar, Phys. Rev. A **95**, 042325 (2017.)

[56] W. Magnus, Commun. Pure Appl. Math. **7**, 649 (1954); S. Blanes, F. Casas, J. Oteo, and J. Ros, Phys. Rep. **470**, 151 (2009).

[57] M. Khezri, Ph.D. thesis, University of California, Riverside (2018), Appendix A.

[58] D. Sank, Z. Chen, M. Khezri, J. Kelly, R. Barends, B. Campbell, Y. Chen, B. Chiaro, A. Dunsworth, A. Fowler, E. Jeffrey, E. Lucero, A. Megrant, J. Mutus, M. Neeley, C. Neill, P. J. J. O'Malley, C. Quintana, P. Roushan, A. Vainsencher, T. White, J. Wenner, A. N. Korotkov, and J. M. Martinis, Phys. Rev. Lett. **117**, 190503 (2016), Supplementary Information.

[59] A. Blais, R. S. Huang, A. Wallraff, S. M. Girvin, and R. J. Schoelkopf, Phys. Rev. A **69**, 062320 (2004).

[60] P. Zanardi and D. A. Lidar, Phys. Rev. A **70**, 012315 (2004).

[61] L. H. Pedersen, N. M. Møller, and K. Mølmer, Phys. Lett. A **367**, 47 (2007).

[62] A. Galiautdinov, A. N. Korotkov, and J. M. Martinis, Phys. Rev. A **85**, 042321 (2012).